A Theoretical and Experimental Investigation on Infrared Metamaterial Absorbers

A THESIS
SUBMITTED TO THE FACULTY OF THE GRADUATE SCHOOL
OF THE UNIVERSITY OF MINNESOTA
BY

WEI JIA

IN PARTIAL FULFILLMENT OF THE REQUIREMENTS
FOR THE DEGREE OF
MASTER OF SCIENCE

JING BAI, DEBAO ZHOU

January, 2020

Acknowledgements

There are many people I want to express my gratitude during my time in graduate school. I would like to thank all my professors, instructors, family, and friends who supported me in any way with this research work.

Especially, I wish to express the utmost gratitude to my advisor, Dr. Jing Bai and my co-advisor, Dr. Debao Zhou for all of their guidance and support through my graduate study. They have provided me with much guidance and support which have allowed me to perform the research necessary for the compilation of this thesis.

I also wish express my sincerely gratitude to Mr. Kevin Roberts and other staff for their support of my experiment research in Minnesota Nano Center.

I truly thank Dr. Mohammed Hasan for his willingness to serve on my thesis committee. Additional, I would like to thank Mia O'Brien for her kindly help to support my academic writing skills.

Finally, I would like to thank all my friends I have made since I came to study at University of Minnesota Duluth.

Dedication

This thesis is dedicated to everyone who supported me financially and mentally throughout my time in graduate school.

Abstract

Metamaterials are artificially engineered structure with unique electromagnetic properties that can not be found in nature. They have many potential applications, and one of its most important applications is metamaterial absorbers. The designing of metamaterial absorbers is based on simultaneous ex citations of an electric dipole and a magnetic dipole resonances. Metamaterial absorber is typically a tri-layer structure with top metallic patterns structured at a sub-wavelength scales, a bottom metallic ground layer and a insulator layer in the middle. The top periodic structure functions as electric resonators driven by the electric field of the incident electromagnetic waves. The magnetic response of the structure is determined by the coupling of the two metallic layers and the dielectric layer. The metallic ground plane needs to be thicker than the skin depth to block any transmission. By altering the geometry sizes of the elements in the structure, the effective permittivity and permeability can be tuned to match the free space impedance, leading to a perfect absorption at certain wavelength.

In the past few years, due to the demands of chemical detection and biological sensing, mid-infrared perfect metamaterial absorbers have been studied. For the broadband metamaterial absorber, we proposed a metal-dielectric-metal structure with top metallic patterns based on uniform raindrop shape. The absorption spectra and electromagnetic field distributions of the structure were numerically calculated by the finite element method based on commercial package COMSOL Multiphysics. Then we designed a braodband metamaterial absorber based on multiple sizes of raindrop shaped resonators. The fabrication of the proposed metamaterial absorbers was performed by E-beam lithography method. Following is the measurement of the absorption spectra using Fourier transform infrared spectrometer and the comparison with simulation results.

Also, a five-band terahertz absorber with high absorbance was proposed and designed. The designed absorber is insensitive to both TE and TM polarization incident waves. The physical origins of the characteristics exhibited by this absorber can be attributed to dipolar and hexapolar resonances, as established by analyzing the electrical field density. Moreover, the influences of the main structural parameters and

configurations on the absorption frequencies were studied. By varying several structural parameters, such as square ring length, dielectric thickness, and cross length, the absorption frequencies can be shifted to higher or lower values. In addition to the adjustment of absorption frequencies, the number of total resonance bands can also be adjusted by revising the structural configurations.

Contents

List of Tables

List of Figures

Chapter 1

Introduction

Electromagnetic metamaterials are artificially structured materials with subwavelength-sized composite arrays of resonant structures which can not be found in nature [9]. The geometrical configuration of each individual unit cell controls its electromagnetic properties. By carefully designing the structure, metamaterials can display electric and magnetic resonances at specific frequencies, which has attracted incredible attention.

1.1 Introduction of Metamaterials

Metamaterials can exhibit extraordinary electromagnetic effects due to the arrays of sub-wavelength elements. The unique properties of metamaterials are induced by the resonances of the sub-wavelength elements. Wave propagation in materials are dominated by materials' properties, which are dielectric permittivity ε, magnetic permeability μ, and conductivity σ. In 1968, Veselago [10] for the first time theoretically studied the propagation of plane waves in materials with negative ε and negative μ. He found that the group velocity propagates in the opposite direction of the Poynting vector in the medium of negative ε and negative μ, which is not the case for conventional materials. In 1999, Smith *et al.* [11] experimentally demonstrated the first material with both negative ε and μ. Later, Pendry [12] explained the existence of negative refractive index. After these works, plenty of research has been conducted in this fields from microwave to optical spectrum regime of electromagnetic waves [13]. Metamaterials can be characterized by effective complex permittivity $\varepsilon(w) = \varepsilon_1(w) + i\varepsilon_2(w)$ and effective

complex permeability $\mu(w) = \mu(w) + i\mu_2(w)$ [2]. By carefully adjusting $\varepsilon(w)$ and $\mu(w)$, it is feasible to construct metamaterials that exhibit properties which are not exist in nature, such as negative index of refraction and backward wave propagation [14]. Typically, metamaterials consist of periodic metallic arrays designed to generate resonances at desired frequency. Unlike conventional materials that depend on material chemical composition, the electromagnetic properties of metamaterials are strongly determines by the structures themselves.

1.2 Metamaterial Absorber

By utilizing the dielectric loss in the metamaterials, high absorption of electromagnetic waves can be achieved in order to exhibit perfect absorption. A perfect metamaterial absorber (PMA) that can achieve perfect absorption of the incident EM waves, was first proposed by Landy *et al.* [1] in 2008. As shown in Figure 1.1, the absorber consists of a metallic split ring, a dielectric layer, and a cut wire. Experimental measurement shows a peak absorption of 88% at frequency 11.5 GHz. The top layer split ring is made of copper and can couple the incident electric field along the ground layer made by copper cut wire at a specific frequency. The top layer and the ground plane are separated by the FR4 dielectric layer. The anti-parallel currents in the top layer and the ground plane generate the magnetic coupling in the FR4 dielectric layer. By tuning the thickness of the dielectric layer and the dimensions of the split ring, specific frequency responses can be achieved. In Figure 1.1, the red line represents the simulation results, and the blue line displays the experimental measurement result.

Changing the thickness of the dielectric layer can alter the magnetic response of the structure. The unit size of the structure can affect the frequency response [15], so the absorption frequency can be tuned by adjusting the structure size. Since Landy proposed this idea, extensive theoretical and experimental research on PMAs has been conducted. The PMA structures have been altered by using a continuous ground metallic plane for simplicity instead of the cut wire reported in Landy's research [1].

Because perfect metamaterial absorbers can be widely used in solar energy harvesting [16, 5], plasmonic sensors [17], micro-bolometers [18, 19], imaging [20, 21], selective thermal emitters [22, 23] and other areas, research on the absorber has been developed

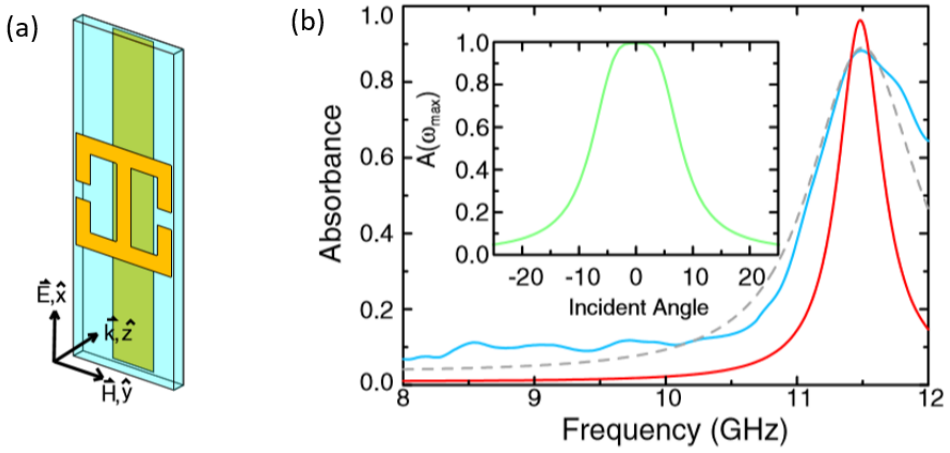

Figure 1.1: Absorber structure and its absorption spectra [1].

rapidly, from the original single-band absorber [1, 24] to the dual-band absorber [4, 25] to the multi-band [26, 27, 28] or even broadband absorbers [29, 30, 31]. In the past few years, the development of mid-infrared absorbers .[32, 33, 34] has been improved due to the needs of sensing and chemical detection.

After Landy proposed the first metamaterial absorber, Tao *et al.* [35] experimentally demonstrated a flexible wide angle incidence of terahertz metamaterial absorber. This absorber consists of two metallic layers separated by two dielectric layers, as shown in Figure 1.2. The top layer is an array of gold solid ring resonators with a thickness of 200 nm. The second gold layer as a ground plane is 200 nm thick. The dielectric layer between the top gold array and the bottom gold ground plane is polyimide with a thickness of 8 μm. The bottom dielectric layer is just the mechanical support of the structure. Figure 1.2 displays the simulated absorption for TE and TM incident radiation with various incident angles from 0° to 80°. For the TE mode, a peak absoption of 99.9% is obtained and remains high absorption for the incident angles increasing to 50°. However for the TM mode, the peak absorption of the absorber is 99.9% and remains higher than 99% for all angles of the incident electromagnetic waves.

In 2010, Tao *et al.* [3] combined two single band electric-field-coupled resonators to achieve a dual band metamaterial absorber. As shown in Figure 1.3, the absorber consists of a electric-field-coupled resonator on the top layer, a metallic ground plane, and dielectric layer in the middle. In Figure 1.3, two distinct absorption peaks can be

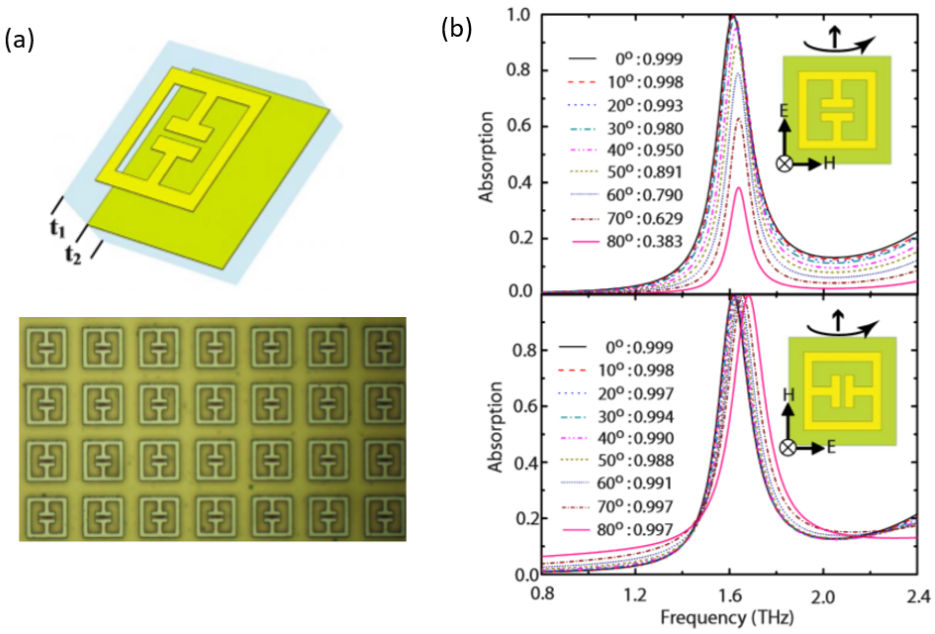

Figure 1.2: Terahertz metamaterial absorber structure and its absorptivity [2].

observed at 1.4 and 3.0 THz. The experimental results matches the simulation results very well. By optimizing the geometries of the corresponding single electric-field-coupled resonator, the two absorption peaks can be tuned individually.

Ma *et al.* [4] designed a dual band terahertz metamaterial absorber. It is a metal-insulator-metal (MIM) structure, as displayed in Figure 1.4. The fabricated absorber was characterized using a Fourier transform IR spectrometer. From Figure 1.4, it clearly shows two distinct absorption peaks at 2.7 and 5.2 THz. The top layer arrays consist of two concentric square rings. Due to its strong magnetic resonance, each square ring can exhibit a distinct absorption peak. By combining them, two distinct absorption peaks can be obtained. Moreover, compared to the structure in Tao *et al.*'s [3], the two square rings structure is symmetric structure in the unit cell, which makes the absorber independent to the polarization of the incident waves.

One of the most effective methods for multiple-band or broadband metamaterial absorbers is to stack different sizes resonator. In 2015, Abul *et al.* [5] designed a absorber based on metallic metasurface structure with broadband and polarization independent properties. The unit cell is complex and consist of multiple pairs of gold nano-resonators.

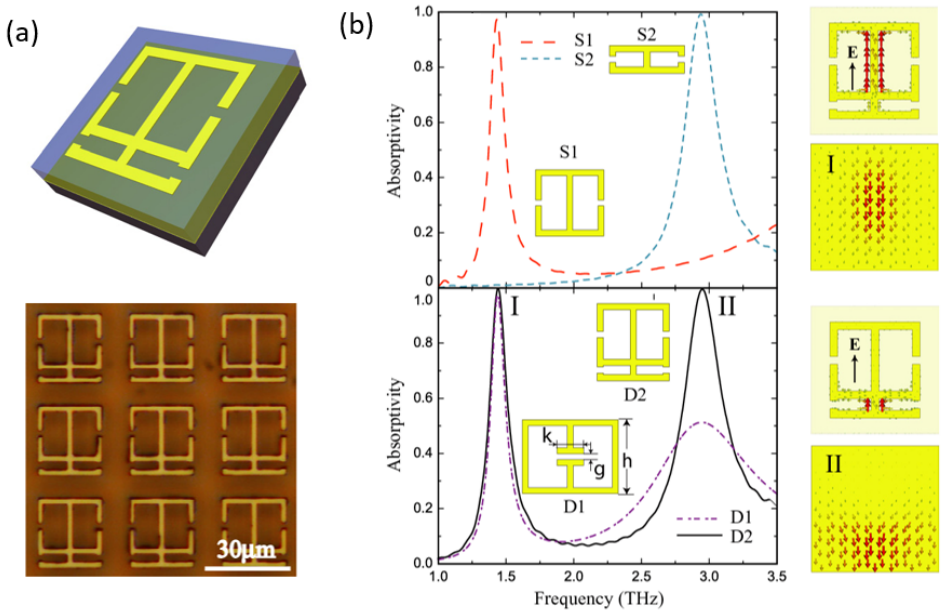

Figure 1.3: Absorber structure and its absorption spectra [3].

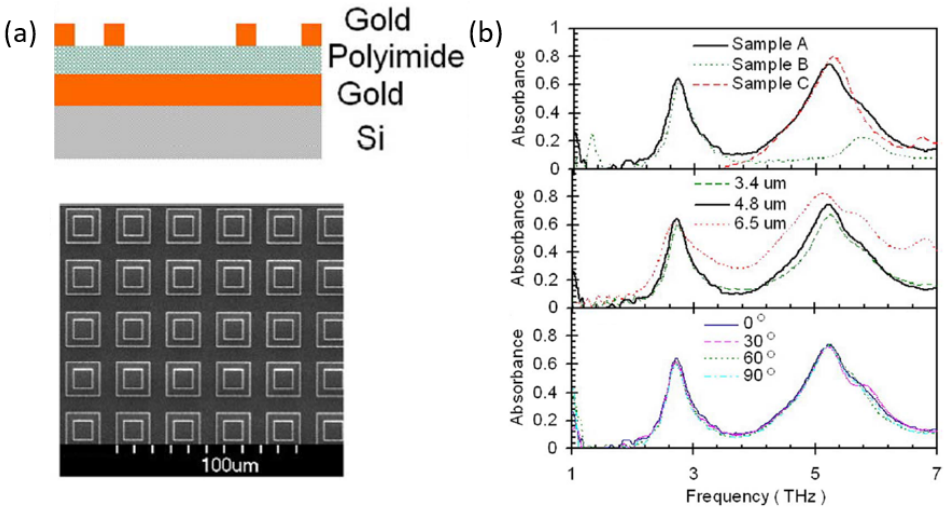

Figure 1.4: Proposed absorber structure and its experimental measurement of absorption [4].

As displayed in Figure 1.5, the experimental measurements reveal high absorption over a wide range of incident angles for both TE and TM polarizations.

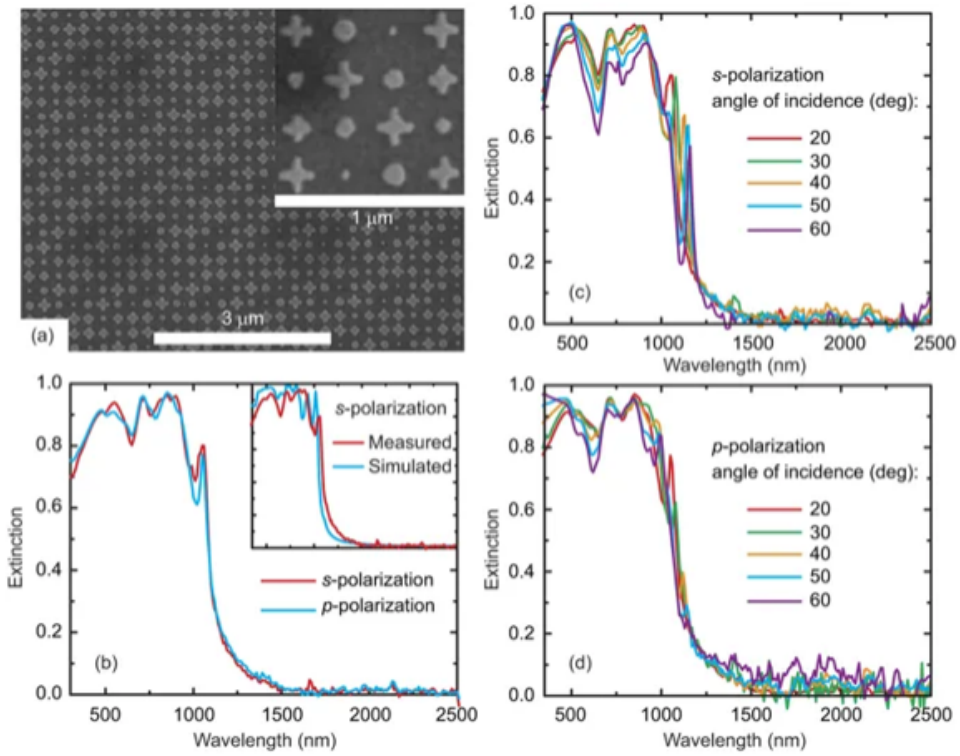

Figure 1.5: Fabricated absorber and extinction spectra [5].

Cui *et al.* [6] proposed a saw-toothed multiple layers metamaterial absorber functioning in the infrared region, as displayed in Figure 1.6. The wavelength absorption band has a full width at half maximum (FWHM) of 86% at norm incident waves. The broad bandwidth of the absorption is achieved by overlapping multiple resonances. Light of higher frequencies is captured by the upper parts of the sawteeth structure, while light of lower frequencies are harvested at the bottom parts.

Multi-layer structures have been demonstrated to generate a broadband absorption greatly in terahertz [24] and microwave [36] regime. Due to the fabrication difficulties, it would be hard to develop a absorber based on multiple layers structures for infrared range. When the sizes of the resonators scale down to micro meters, the lithography and alignment of multiple layers will be hard to achieve.

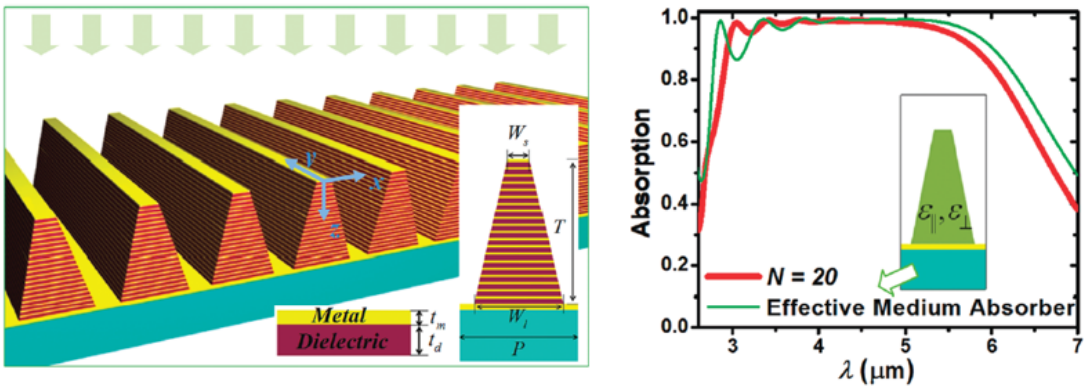

Figure 1.6: Saw-toothed metamaterial absorber structrue and its absorption spectrum [6].

For infrared range, some researchers have proposed broadband metamaterial absorbers based on using two different sizes square shape resonators [37] or even four different sizes circular shape resonators[38] and cross shape resonators [39]. However, a broadband metamaterial absorber based on raindrop shaped resonators has rarely been reported.

1.3 Research objectives and thesis outlines

1.3.1 Research objectives

The objective is to design a broadband metamaterail absorber functioning in infrared regime. The novel structure is based on raindrop shape resonator, which is different from common circular, square or cross shape, etc. and has not been proposed before. By combine multiple sizes raindrop shaped resonators on the top layer, a wide band absorption in infrared regime can be realized. Also, experimental fabrication based on E-beam lithography of the proposed metamaterial absorbers is proceed to verify the simulation results carried by COMSOL Multiphysics.

Also, in order to design a adjustable high-absorption multiple bands metamaterial absorber to be beneficial in a lot of engineering fields, such as detecting and terahertz imaging, a structure that can generated five absortion bands in the terahertz regime is

proposed. The structure is MIM based structure and consists of a cross and four quarter-sectional circular rings surrounded by a square ring within the top layer. The number of total resonance bands can be adjusted by revising the structural configurations.

1.3.2 Thesis outlines

- Chapter 1 introduces the development of metamaterial absorbers and the goals pursued in this thesis.
- Chapter 2 presents the theoretical background of metamaterial absorbers and the finite element method and its implementation in COMSOL. The simulation method in COMSOL is also verified by simulation a proposed metamaterial absorber in a reference paper.
- In Chapter 3, different shape of resonators is studied and an idea to generate a broadband absorption metamaterial absorber based on raindrop shape resonators is proposed. The simulation results of the proposed broadband absorber functioning in infrared region is analysed.
- Chapter 4 describes the experimental realization of the proposed absorbers based on E-beam lithography method .
- In Chapter 5, a five-band terahertz metamaterial absorber with a flexible structure is described and analyzed.
- Chapter 6 presents the final conclusions and future works.

Chapter 2

Metamaterial background

2.1 Electromagnetic Theory

The electromagnetic responses of materials to EM waves are critically determined by the material permittivity ε and permeability μ. They play a important role in the EM waves propagation in the medium. The electric permittivity determines the interactions of the medium and electric fields while the magnetic permeability defines the reactions of materials to applied magnetic fields. Because the structure in each unit has sub-wavelength dimensions, the incident electromagnetic waves have effects on the overall patterns instead of the single structure. Therefore, sub-wavelength periodic arrays can be considered as a media with effective electric permittivity and effective magnetic permeability.

The interactions between the incident electromagnetic waves and the structures can be formulated using Maxwell equations. Maxwell equations form the basis of all matter and light interactions. In 1865, James Clerk Maxwell [40] devised four main equations, which are shown by following:

$$\text{Gauss's Law:} \quad \nabla \cdot \overrightarrow{D} = \rho \tag{2.1}$$

$$\text{Gauss's Law for Magnetism:} \quad \nabla \cdot \overrightarrow{B} = 0 \tag{2.2}$$

$$\text{Faraday's Law of Induction:} \quad \nabla \times \overrightarrow{E} = -\frac{\partial \overrightarrow{B}}{\partial t} \tag{2.3}$$

$$\text{Ampere's Circuital Law:} \quad \nabla \times \overrightarrow{H} = \frac{\partial \overrightarrow{D}}{\partial t} + \overrightarrow{J} \tag{2.4}$$

where $\overrightarrow{E}$ is the electric field intensity ($V.m^{-1}$), $\overrightarrow{H}$ is the magnetic field intensity ($A.m^{-1}$),

$\overrightarrow{D}$ is the electric flux density (C/m^2), $\overrightarrow{B}$ is the magnetic flux density (Wb/m^2), $\overrightarrow{J}$ is the electric current density (A/m). While in a source-free medium, there is no net charge and no current, so ρ=0, $\overrightarrow{J}$=0. Also, in a isotropic and homogeneous medium, the electromagnetic constitutive relationships are expressed as following:

$$\overrightarrow{D} = \varepsilon_0 \overrightarrow{E} + \overrightarrow{P} = \varepsilon_0 (1 + \chi_e) \overrightarrow{E} = \varepsilon_r \varepsilon_0 \overrightarrow{E} = \varepsilon \overrightarrow{E} \tag{2.5}$$

$$\overrightarrow{B} = \mu \left(\overrightarrow{H} + \overrightarrow{M} \right) = \mu (1 + \chi_m) \overrightarrow{H} = \mu_r \mu_0 \overrightarrow{H} = \mu \overrightarrow{H} \tag{2.6}$$

where ε, ε_r and ε_0 are the electric permittivity of absolute, relative and free space respectively, and μ, μ_r and μ_0 are the magnetic permeability of absolute, relative and free space respectively. σ is the conductivity expressed in S/m, χ_e is the electric susceptibility, and χ_m is the magnetic susceptibility. Thus, we can rewrite the Maxwell equations as:

$$\nabla \cdot \varepsilon \overrightarrow{E} = 0 \tag{2.7}$$

$$\nabla \cdot \mu \overrightarrow{H} = 0 \tag{2.8}$$

$$\nabla \times \overrightarrow{E} = -\mu \frac{\partial \overrightarrow{H}}{\partial t} \tag{2.9}$$

$$\nabla \times \overrightarrow{H} = \varepsilon \frac{\partial \overrightarrow{E}}{\partial t} \tag{2.10}$$

With electromagnetic field $\overrightarrow{E} = E_0 e^{-iwt}$ and $\overrightarrow{H} = H_0 e^{-iwt}$, substitute into the above equations, we can get:

$$\nabla \times \overrightarrow{E} = i\omega \mu \overrightarrow{H} \tag{2.11}$$

$$\nabla \times \overrightarrow{H} = -i\omega \varepsilon \overrightarrow{E} \tag{2.12}$$

Then, the wave equation for a isotropic and homogeneous medium can be derived as following:

$$\nabla \times \left(\nabla \times \overrightarrow{E} \right) - k^2 \overrightarrow{E} = 0 \tag{2.13}$$

where $k = nk_0$ is the wave number, k_0 is the wave number of free space, n is the refractive index of the medium which are defined as following:

$$n = \sqrt{\varepsilon_r \mu_r} \tag{2.14}$$

Generally, permittivity and permeability can be expressed to be complex and dispersive as function of frequency, i.e. $\varepsilon(w) = \varepsilon_1(w) + i\varepsilon_2(w)$ and $\mu(w) = \mu(w) + i\mu_2(w)$. so the wave impedance can be expressed as following:

$$Z = \sqrt{\frac{\mu}{\varepsilon}} \tag{2.15}$$

Most materials that exist in nature are characterized by positive ε and μ. A negative index of refraction can be obtained if ε and μ are simultaneously negative. A material with negative index of refraction is known as left-handed material and exhibits backward wave propagation, i.e. the wave vector is opposite to the poynting vector, as shown in Figure 2.1.

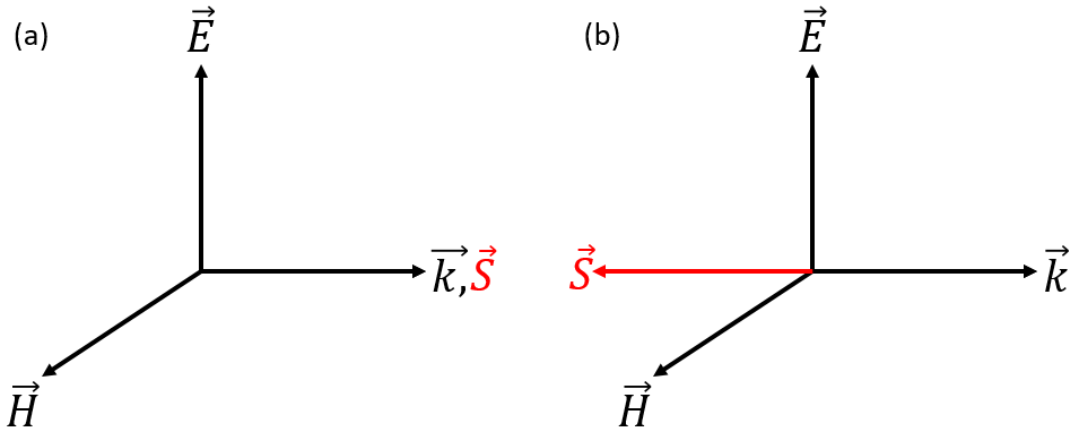

Figure 2.1: (a) Right-handed media: $\vec{S}$ and $\vec{k}$ in same direction. (b) Left-handed media: $\vec{S}$ and $\vec{k}$ in opposite direction.

The permittivity and permeability of materials are essential to predict the electromagnetic response. The materials performance to electromagnetic fields are thoroughly determined by the values of them. Figure 2.2 shows four possible combinations ε and μ of materials .

I.$\varepsilon > 0, \mu > 0$: A medium satisfies this condition is called double positive medium (DPM). Electromagnetic waves can propagate through the media with both positive permittivity and permeability. If the medium has complex permittivity, waves will propagate and decay in the medium.

II.$\varepsilon < 0, \mu > 0$: A medium with negative permittivity and positive permeability is

termed as epsilon negative (ENG) material. Many plasmas display this characteristic. Noble metals are common ENGs in the infrared and visible frequency region.

III.$\varepsilon < 0, \mu < 0$: A medium that has both negative permittivity and permeability is named a double negative (DNG) medium. It is also called left-handed medium. Media with this property do not exit in nature. They have been demonstrated in artificial structures. The direction of the wave propagation is opposite to the wave poynting vector ($\vec{E} \times \vec{H}$).

IV.$\varepsilon > 0, \mu < 0$: Materials with positive permittivity and negative permeability can decay incident waves evanescently and can not sustain propagation modes. They are called permeability negative (MNG) media. Some ferromagnetic materials with resonances in microwave region have this phenomenon.

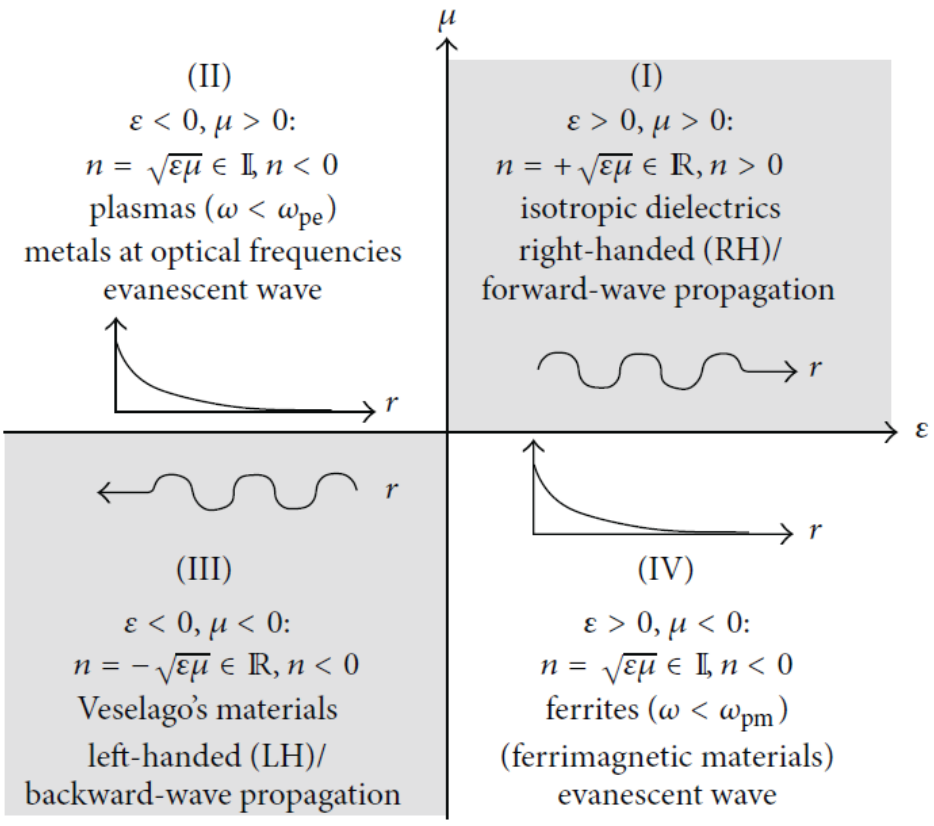

Figure 2.2: Combinations of materials electric permittivity and magnetic permeability [7]

2.2 Absorption equation and impedance matching

In order to calculate the absorption properties of the absorbers, the following equation is used [41]:

$$A(\omega) = 1 - R(\omega) - T(\omega) = 1 - S_{11}^2 - S_{21}^2 \tag{2.16}$$

where A(ω) = absorption; R(ω) = reflection = $|S_{11}|^2$; T(ω) = transmission = $|S_{21}|^2$; $S_{11}(\omega)$= scattering parameter of reflection; $S_{21}(\omega)$= scattering parameter of transmission. In simulations, the S-parameters are calculated from the power flow through the ports, which are given by the following equations [42]:

$$S_{11} = \frac{\sqrt{Power \quad reflected \quad from \quad port \quad 1}}{\sqrt{Power \quad incident \quad on \quad port \quad 1}} \tag{2.17}$$

$$S_{21} = \frac{\sqrt{Power \quad delivered \quad to \quad port \quad 2}}{\sqrt{Power \quad incident \quad on \quad port \quad 1}} \tag{2.18}$$

Due to the existence of the ground plane on the bottom layer, with thickness greater than the skin depth, the transmission through the structure can be effectively suppressed, which indicates $S_{21}(\omega)$= 0. So the absorption equation can be altered to the following:

$$A(\omega) = 1 - R(\omega) = 1 - S_{11}^2 \tag{2.19}$$

To achieve perfect absorption without reflection, the surface impedance of the whole structure should be constructed in a way to match to the intrinsic impedance in free space [43]. The free space impedance can be calculated by the following equations [44]

$$Z_0 = \sqrt{\frac{\mu_0}{\varepsilon_0}} = \sqrt{\frac{4\pi \cdot 10^{-7}}{10^7/4\pi c^2}} = 377\Omega \tag{2.20}$$

where Z_0 is free space impedance, $\varepsilon_0 = 10^7/4\pi c^2\ Fm^{-1}$ is the permittivity of the free space, $\mu_0 = 4\pi \cdot 10^{-7}\ Hm^{-1}$ is the permeability of the free space.

The surface impedance $Z(\omega)$ of the structure is calculated by the following equations [45]:

$$Z(\omega) = Z_0\sqrt{\frac{\mu_r(\omega)}{\varepsilon_r(\omega)}} = Z_0 \tag{2.21}$$

where $\mu_r(\omega) = \mu_1 + i\mu_2$ is the complex relative magnetic permeability, and $\varepsilon_r(\omega) = \varepsilon_1 + i\varepsilon_2$ is the complex relative electric permittivity. By tuning of the resonance to achieve equivalent permittivity and permeability, the impedance of metamaterial can match the free space impedance, the maximum absorption can be achieved once the following condition established:

$$|S_{11}(\omega)| = \left| \frac{Z(\omega) - Z_0}{Z(\omega) + Z_0} \right| = 0 \tag{2.22}$$

2.3 FEM and its implementation in COMSOL

Due to the existence of the advanced numerical simulation techniques, we are able to use the numerical method to design and optimize the geometrical parameters of the metamaterial absorber. Numerical simulations have been developed as a powerful method to design and optimize the structure and predict its behavior without fabrication iterations. Moreover, it can reveal a lot of phenomena of the structures which can not be fully observed by experimental measurements.

Commercial finite element software COMSOL Multiphysics was used to perform the full-wave three-dimensional simulations and study the EM properties of the proposed MA structures. The finite element method (FEM) that can handle complex materials and geometries is described by partial differential equations and widely used in electromagnetic calculation areas. The basic idea of FEM is to divide a continuous physical structure into small and finite elements. The corner points of each elements are called nodes. The unknown functions of these nodes need to be determined. By using the nodal values, the values inside the finite elements can be recovered. For MA simulations in COMSOL Multiphysicals, the following are the basic modeling steps.

I. Defining the MA parameters and structure. COMSOL provides two ways to define constants and expressions: one is global definitions and the other one local definitions. Depending on the types of constants and expressions, one can choose to use local or global definitions for convenience. The software has a built-in geometry module which can be used to perform 2-D and 3-D modeling, such as block, cone, cylinder, sphere, etc. Booleans and partitions, such as union, intersection, difference and compose, can be used for modeling irregular structures. The 3-D unit cell MIM MA structure is shown in Figure 2.3. The unit cell consists of a metal ground plane on the bottom, a

metallic raindrop disk above the ground plan, separated by a dielectric layer. Above the raindrop disk is the air layer. Perfectly matched layers(PML) are placed on the top of the structure to absorb all outgoing waves.

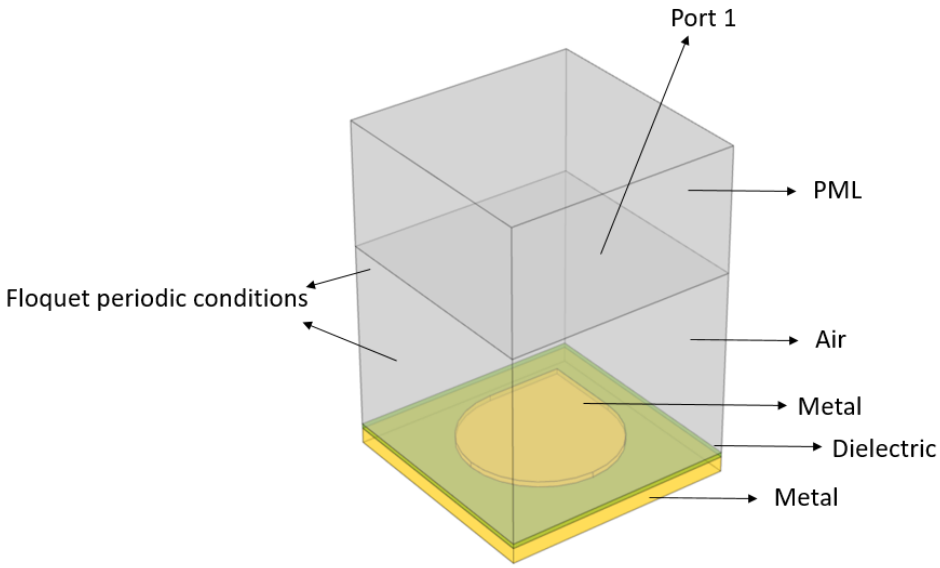

Figure 2.3: 3-D Unit cell structure of metamaterial absorber

II. Setting the sub domains. The unit cell of the whole structure is divided into different sub domains. In each sub domain, one can define the materials properties. The refractive index, permittivity, permeability, etc. can be defined from material library in COMSOL or specified by the user. PML is defined on the top domain to absorb any reflection from the exterior boundaries.

III. Setting boundaries. One can only simulate one unit cell of the MA structure by applying periodic boundary conditions to four vertical sides. Here, Floquet periodic conditions are applied. Between the interface of the PML domain and air domain is set to be port boundary condition. The port condition can specify the incident wave and compute reflection coefficients. To determine the reflection of the structure, the S-parameter from the port boundary condition is used. Following is the formula for the S-parameters:

$$S_{11} = \frac{\int_{port1} \left((E_c - E_r) \cdot Er^* \right) dA_1}{\int_{port1} \left(E_r \cdot Er^* \right) dA_1} \tag{2.23}$$

where E_c and E_r are the electric patterns on port 1.

IV. Meshing. The mesh module has multiple mesh elements for users to choose, such as tetrahedral, hexahedral, pyramid and etc.. The mesh sizes can be controlled by the user defined parameters under the mesh interactive window. Each domain can have its own mesh elements and mesh sizes. Due to strong field enhancement near the MIM layers, the mesh sizes are more refined within the layers in order to achieve higher accuracy.

Finally, Solving. The PARDISO solver is chosen for the calculation. Compared to other direct solves, such as SPOOLES, the PARDISO solver is more efficient and robust for linear systems of equations. The parametric sweep function is used to calculate absorptions of the structure under different wavelengths.

2.4 Simulation Method Verification

Fei Ding *et al.* [8] reported broadband near-infared metamaterial absorbers for near infrared frequencies. Their simulation results clearly show that three prominent absorption peaks at locations 635 nm, 730 nm, and 1965 nm can be clearly observed.

Commercial finite element software COMSOL Multiphysics is used to validate the accuracy of the model with the theoretical observations. Figure 2.4 shows the structure and the absorption spectra of the simulated model. In the simulation test, a size of the square unit cell of the metamaterial absorber is set to 600 nm. The diameter of the top gold disk is 400 nm. The thicknesses of the top gold layer and the bottom gold layer are 30 nm and 100 nm, respectively, separated by a 160 nm thin film middle layer SiO_2. Periodic boundary conditions are applied on the vertical sides. The incident wave is set to be the plane wave norm to the top surface with the polarization along x direction.

The absorption spectra are calculated by performing COMSOL Multiphysics. As shown is Figure 2.5, the calculated absorption spectra shows similar trends as displayed in reference [8].

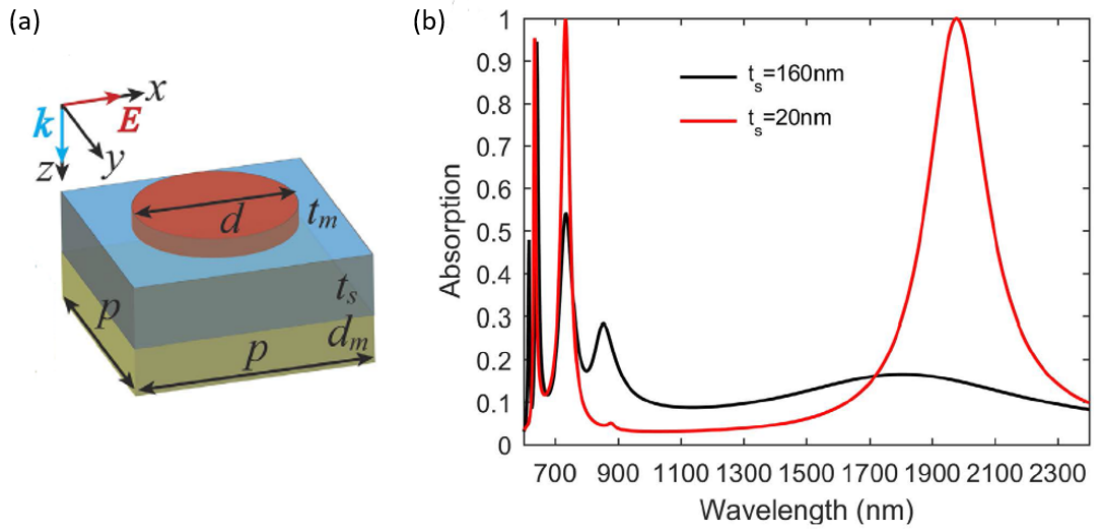

Figure 2.4: Schematic of the perfect infrared broadband absorber with its simulated absorption spectra [8].

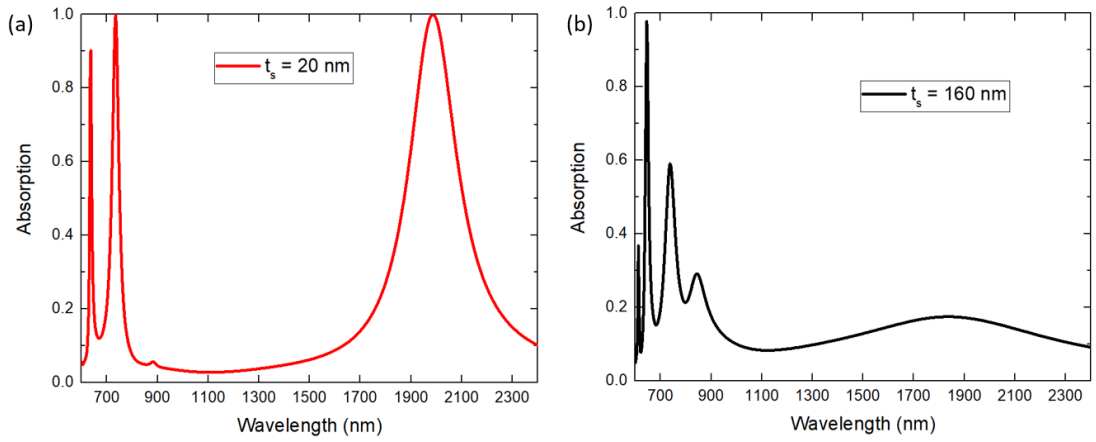

Figure 2.5: Simulated absorption spectra with SiO_2 thickness (a) 20 nm, (b) 160 nm.

Chapter 3

Design of Broadband Metamaterial Absorbers for Infrared Frequencies

3.1 Introduction

In this chapter, we first studied and analysed the effects of different shaped resonators on the absorption properties. Also, a new array pattern for the top layer based on raindrop shape is proposed. While the most popular shape has been circular, we transformed the design into a raindrop shape. As opposed of the full symmetricity of a circular shape, we aligned the raindrop to be symmetric along the 45° line. Based on our theoretical exploration of tailoring the symmetricity and uniformity of the metallic micron raindrop shaped disk on the top, the absorption band can be broadened. By changing the circular shape to raindrop shape, the MIM based absorber has been predicted to generate two absorption peaks with significantly broadened absorption bandwidth. Subsequently, we found that even wider spectra could be achieved if the top layer is built with a periodic arrangement of the unit cells containing differently sized raindrop-shaped disks. This leads to a wider bandwidth of higher than 50% absorbance ranging from 2.80 μm to 3.90 μm.

3.2 Metamaterial absorbers with varied shape

3.2.1 Circular disk, square and cross shaped resonators

As the first step of our study, we studied the MIM structure with the top layer filled with a uniform arrangement of circular, square and cross disks. Figure 3.1 shows the unit cell schematic of three different shapes of MA structure. For the structure we adopted in our modeling, the thickness of the gold ground plane on the bottom is 100 nm and the thickness of the periodic gold arrays on the top is 45 nm, separated by 60 nm dielectric spacer SiO_2 with a constant refractive index of 1.45, which is considered to be lossless [8]. The period length $p1$ of each cell is set to be 1.5 μm. The related structure parameters are shown in Table 3.1. A Lorentz-Drude model was used for the gold material [46]. The incident wave was set to be plane waves parallel to the X-Z plane with TE polarized along the Y direction. Periodical boundary conditions were applied on the vertical sides of the structures. Port boundary condition was used between the interference of the PML layer and air layer. The wavelength dependent reflection parameter R(λ) was obtained from the S-parameter of the port and the absorption of the structure was calculated by A(λ) = 1 - R(λ). Due to the exist of the bottom ground layer, which is thicker than the skin depth at the desired wavelength range, the total transmission is close to zero.

Table 3.1: Structure parameters (unit: nm)

d	a	p	t1	t2	t3
1000	500	1500	45	60	100

3.2.2 Absorption properties analysis

Figure 3.2 shows the simulated absorption spectra of structures with different top metallic arrays. The incident EM waves are parallel with X-Z plane and normal to the surface with TE polarized along Y direction. The absorption peak for circular, square and cross shapes are 3.72, 4.38 and 3.90 μm respectively. In order to further understand the physic origins of the absorbers, the electric field and magnetic field distributions are investigated.

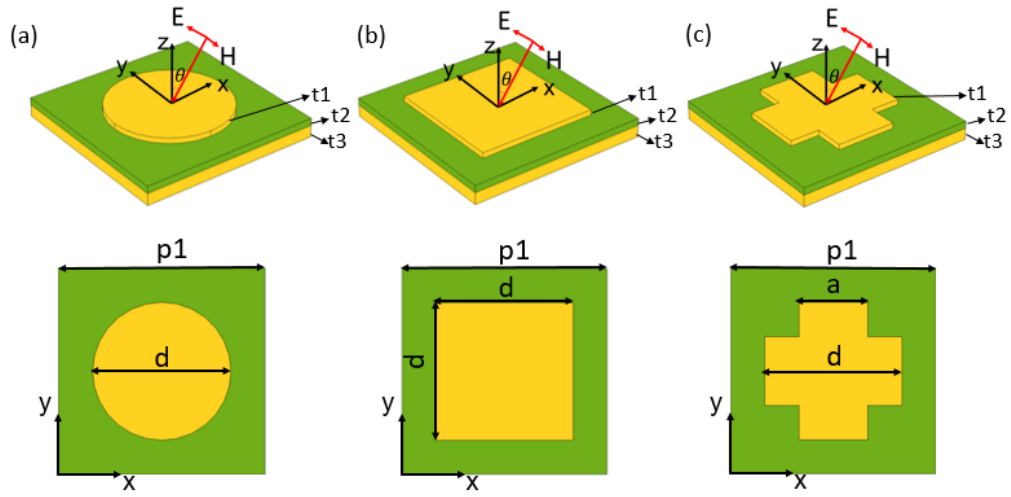

Figure 3.1: Schematic unit cell structure of three different shapes: (a) circular, (b) square, (c) cross.

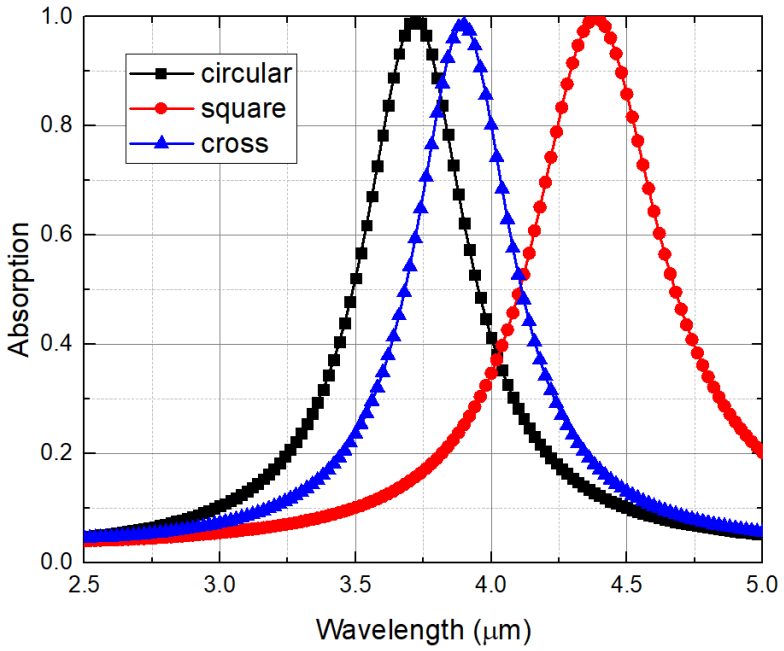

Figure 3.2: Simulated absorption spectra of structures with different top metallic arrays.

Figure 3.3 shows the electric field distribution at the interface of top metallic resonators and the dielectric layer at each resonance wavelength. The electric field distributions in Figure 3.3 clearly display the excitation of an electric dipole resonance at the resonant wavelength. Figure 3.4 shows the magnetic field distribution of the Z-Y cross section of the structure, and Figures 3.5(a),(b), and (c) display the magnetic field distribution of the cross section along the X-Y plane. Figures 3.5(d),(e), and (f) show the current flow directions of different shape structures. As shown in Figure 3.4, the magnetic field is strongly excited in the dielectric layer between the top and bottom metallic layers. From Figures 3.5(d),(e), and (f), opposite oriented currents are formed in the top metallic patterns and bottom metallic ground plane. The induced anti-parallel currents in the top metallic patterns and bottom metallic ground plane yield strong localization magnetic field in the dielectric layer. This circulating current is known as magnetic resonance [47], resulting in an artificial magnetic moment that strongly interact with the magnetic field of the incident EM waves. As shown in Figure 3.5(a),(b), and (c), the magnetic field is strongest between the top metallic patterns and bottom metallic ground plane. As a result, the energy from incident EM waves can be efficiently trapped in the dielectric layer.

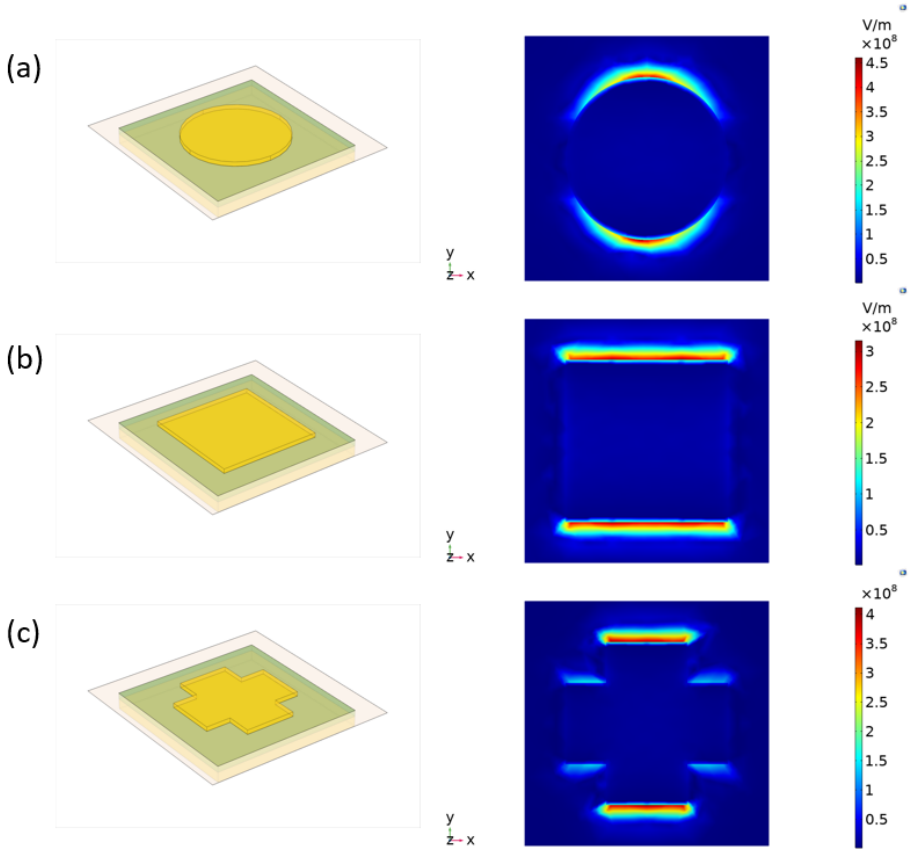

Figure 3.3: Electric field distribution $|E_y|$ at the interface of the top metallic resonators and dielectric layer at the resonant wavelength of different shape resonators: (a) circular disk; (b) square; (c) cross.

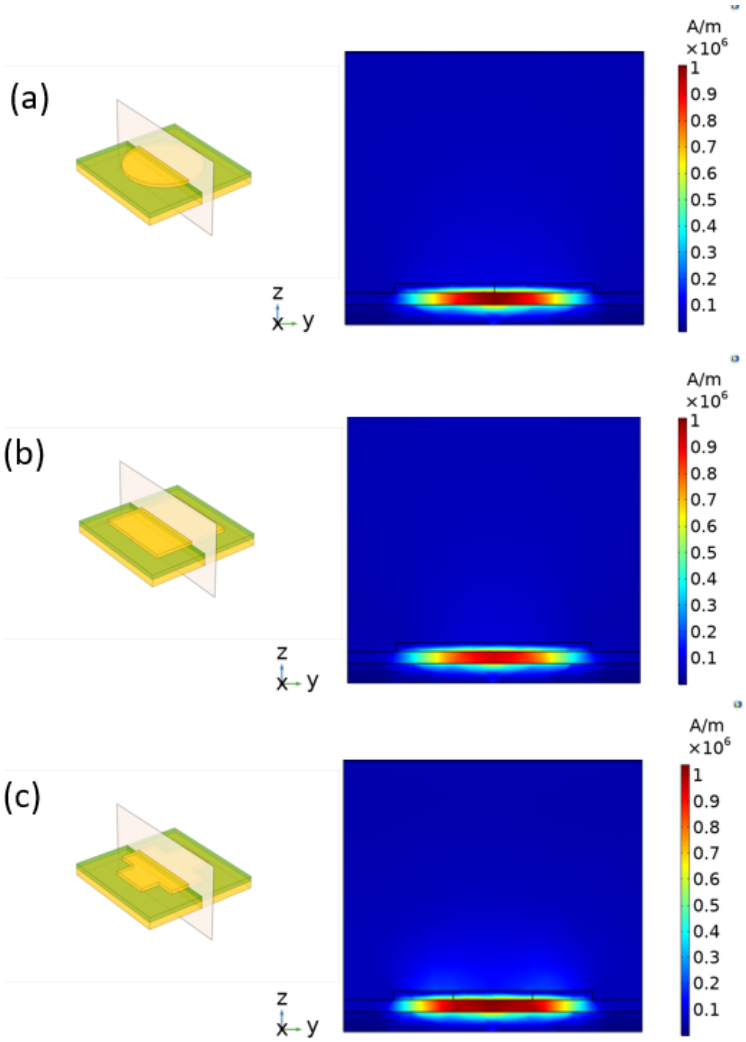

Figure 3.4: Magnetic field distribution $|Hx|$ at the resonant wavelength of different shape resonators: (a) circular disk; (b) square; (c) cross.

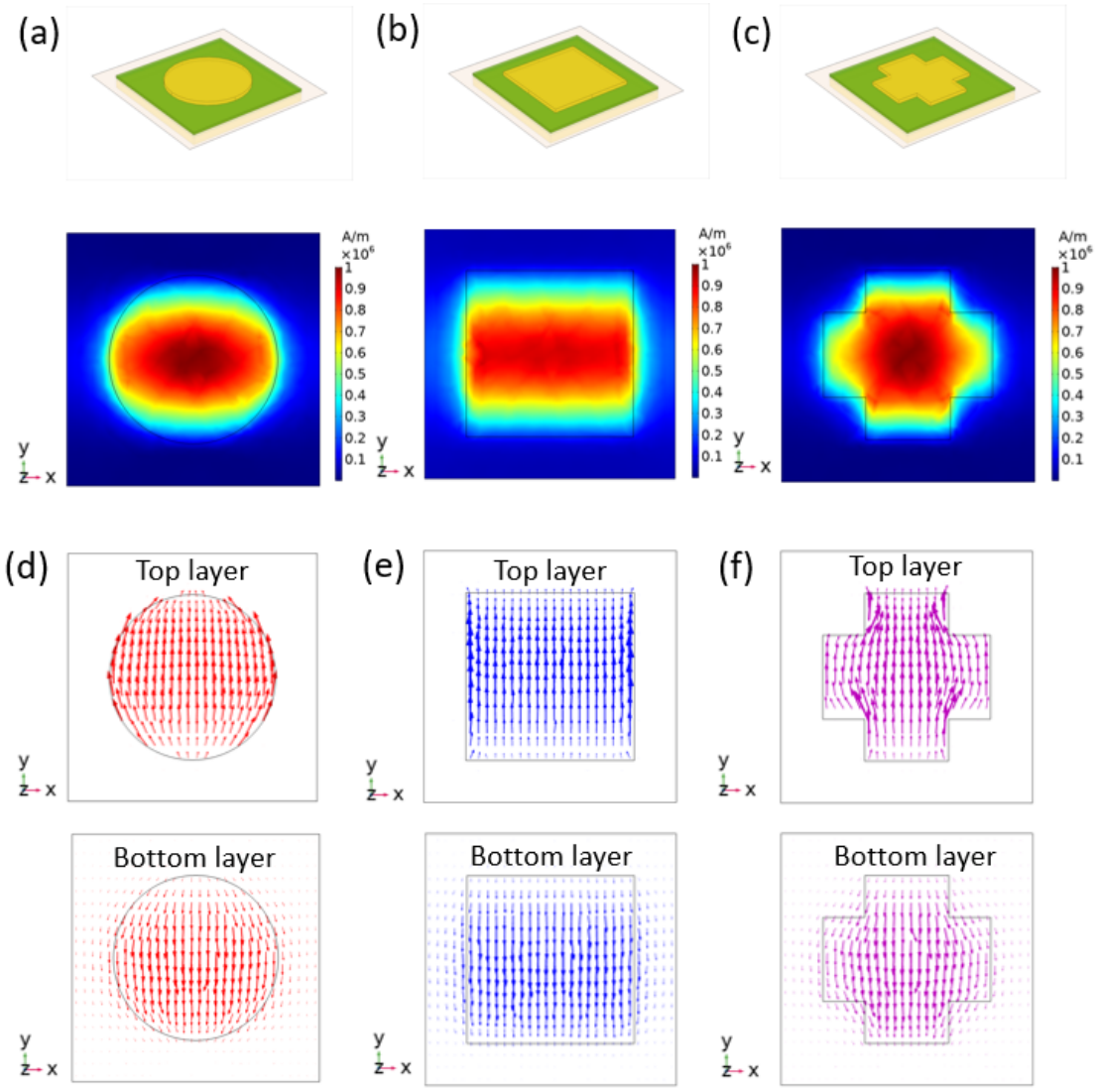

Figure 3.5: Magnetic field distribution $|Hx|$ at the resonant wavelength of different shape resonators at the cross section of the dielectric layer: (a) circular disk; (b) square; (c) cross. Current flow direction in the resonators and bottom ground plane: (d) circular disk; (e) square; (f) cross.

3.3 Uniform raindrop shaped resonators

3.3.1 Uniform raindrop shaped resonators with same pointing directions

For the top layer of circular resonator, replacing the upper right quarter of the circle disk by a square disk can generate a broadband absorption. Figure 3.6 shows the schematic unit cell structure of the raindrop resonator. The radius d is 1000 nm, and the rest parameters are same as previous resonators.

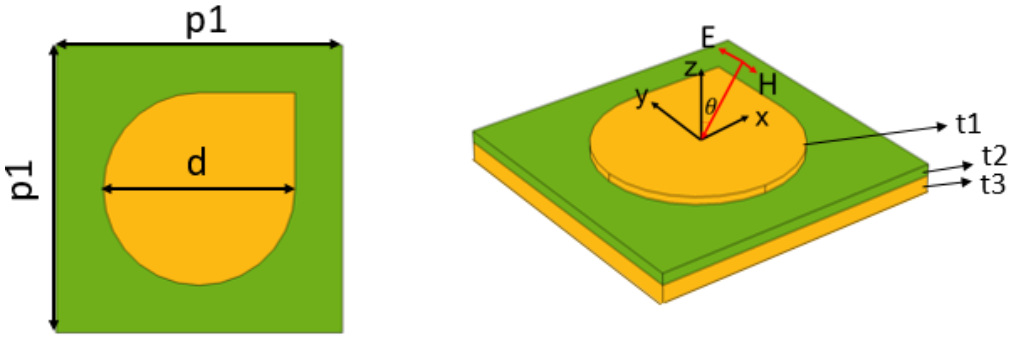

Figure 3.6: Schematic unit cell structure of the raindrop resonator.

Figure 3.7 shows the absorption spectra of raindrop shape resonator and circular disk resonator. From Figure 3.7, as the black curve shows, we can clearly see that the circular disk resonator exhibits only one absorption peak at the wavelength of 3.72 μm with absorption intensity reaches to 99.8%. Meanwhile, the raindrop shape resonator presents two absorption peaks with the absorption of 90.0% and 86.5% at the wavelength of 3.75 μm and 4.02 μm respectively, which is shown as the red curve in Figure 3.7. The FWHM with respect to the center frequency of the circular disk resonator is 12.1% from 3.50 μm to 3.95 μm. While for raindrop absorption spectrum, as the red curve shows, the FWHM of the raindrop shape resonator is 21.0% from 3.50 μm to 4.32 μm.

Figure 3.8 shows the electric field distribution $|E_y|$ at the interference of the dielectric layer and the raindrop shaped resonators. The electric field distribution at two chosen resonant wavelengths 3.75 μm and 4.02 μm are shown in Figure 3.8(b) and (c) respectively. We can clearly tell from the electric field distribution that the electric dipole

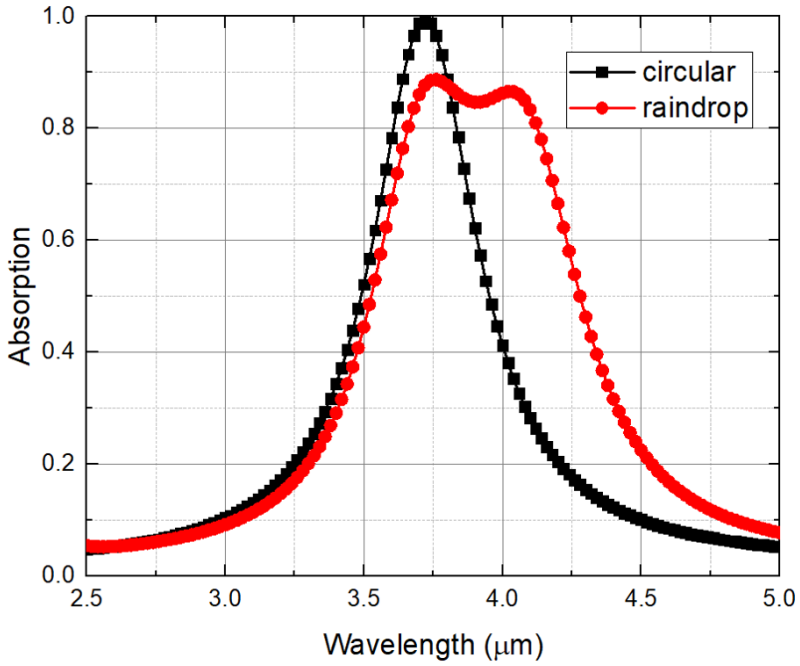

Figure 3.7: Simulated absorption spectra of circular disk and raindrop shape resonators.

resonance was excited at resonant wavelength of 3.75 μm due to the circular shape part, as shown in Figure 3.8(b). And another electric dipole resonance was excited at the wavelength of 4.02 μm, which was caused by the exsit of the right upper square shape, as shown in Figure 3.8(c). So, for raindrop shape resonator, two dipole resonance can be excited by the electric field of the incident EM waves compared to the circular disk resonators.

Figure 3.9 shows the magnetic field distributions at the two absorption peaks at the wavelenths of 3.75 μm and 4.02 μm. And Figure 3.10 shows the corresponding current density at the wavelenths of 3.75 μm and 4.02 μm. From Figure 3.9, it clearly shows the magnetic fields distrubution is localized and strongest in the dielectric layer. Driven by the magnetic field of the incident EM waves, the magnetic dipole resonance was induced between raindrop resonators and the ground plane with anti-parallel currents formed between them, as shown in Figure 3.10. In Figure 3.10(a), at resonat wavelength 3.75 μm, shown by the blue arrows, the current flows from right to left in the raindrop resonators, while in the bottom ground plane, the current flows from left to right. It

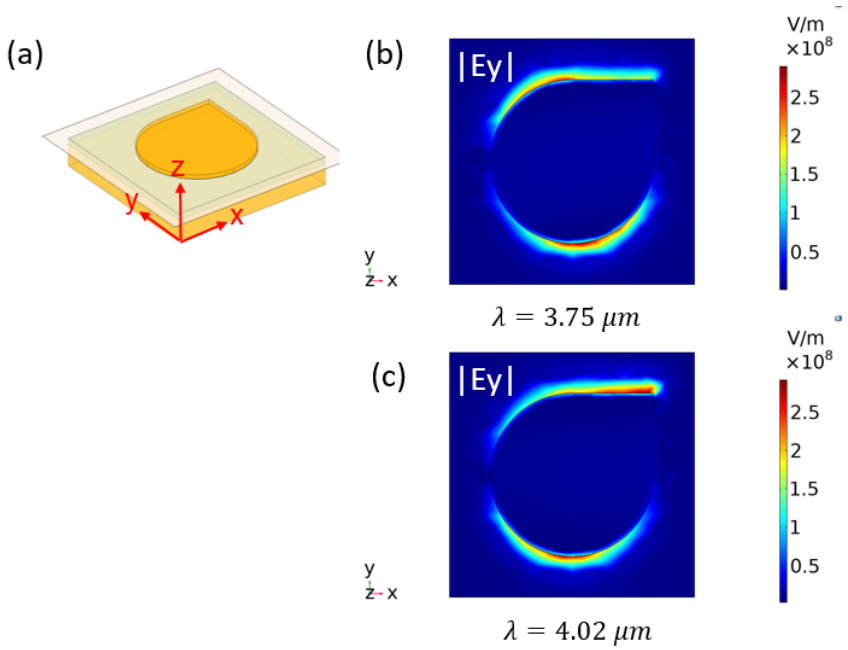

Figure 3.8: The electric field distributions at the interference of the dielectric layer and raindrop resonators

is clear to tell that the current flow direction are opposite in the raindrop layer and bottom ground plane, which results in the magnetic field in the dielectric layer. While at resonant wavelength 4.02 μm, similar phenomenon can be observed from Figures 3.10. The induced currents can result in a magnetic dipole moment to interact with the magnetic field of the incident waves [48].If the electric dipole resonance and magnetic dipole resonance occur at the same frequency, the metamaterial structure will obtain strong localization of elctromagnetic energy. Perfect absorption can be achieved by tuning the resoance frequency of optical impedance to match free space impedance. In order to achieve perfect absorption for the raindrop shape resonator, the thickness of the SiO_2 layer needs to be further adjusted.

However, the raindrop shape resonator with same pointing direction will only have one line of symmetry, which aligns 45° with x axis. So the structure is sensitive to the azimuthal angles of the incident waves. The absorption spectra with different azimuthal angles under normal incidence are shown in Figure 3.11. The incident wave is set to be plane wave in xz plane with TE polarized along y direction. From the Figure 3.11, it

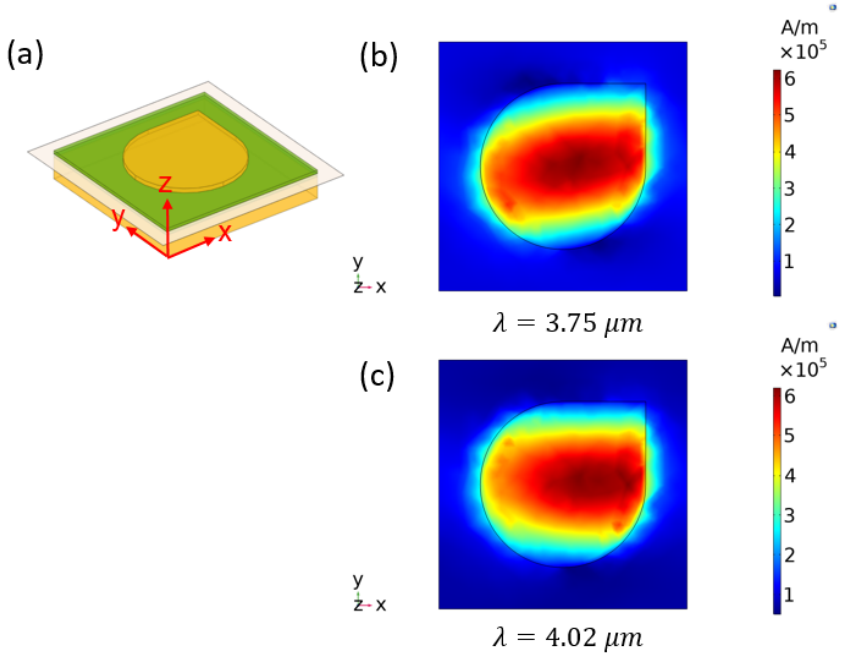

Figure 3.9: The magnetic field distributions $|H_x|$ at two absorption peaks.

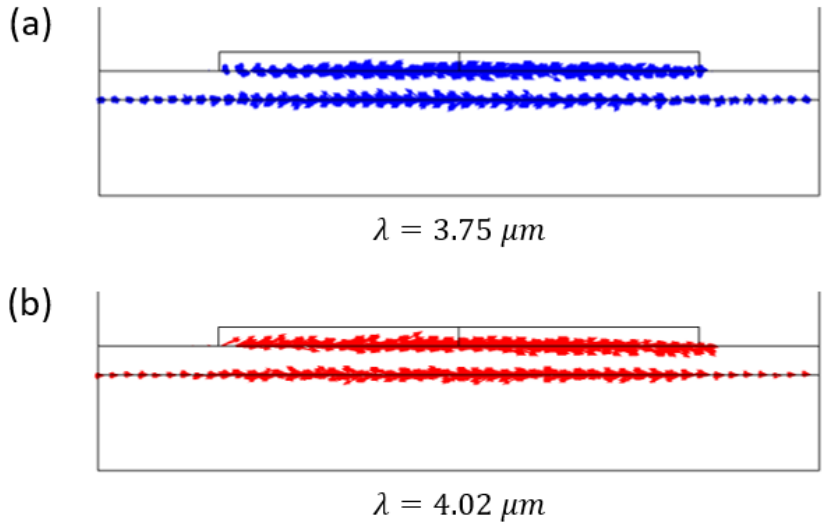

Figure 3.10: Surface current density of the cross section.

can be see that only one absorption peak is achieved when the azimuthal angle is set to be 45°. So the configuration of the structure needs to be reconstructed in order to make the unit cell has more symmetries.

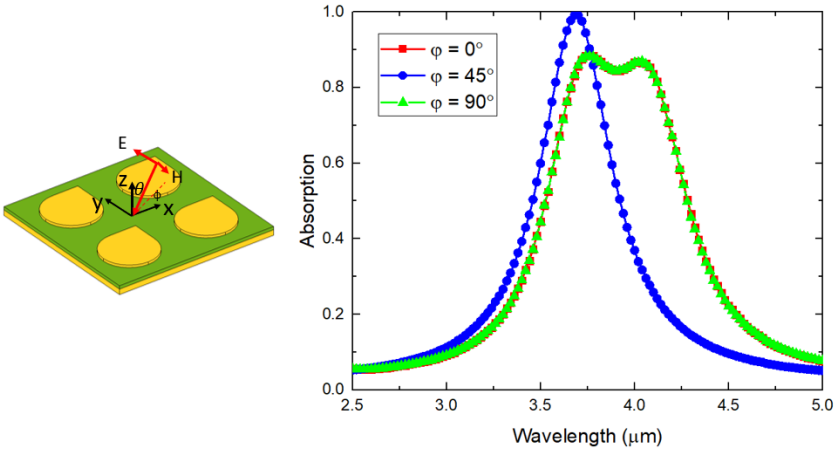

Figure 3.11: Absorption spectra with different azimuthal angles under normal incidence.

3.3.2 Uniform raindrop shaped resonators with different pointing directions

In order to make the absorber insensitive to the azimuthal angles of the incident angles, four same size raindrop shaped resonators are combined into one unit cell with pointing directions outward to each corners of the unit cell, as shown in Figure 3.12. The period length p of each cell is set to be 3.0 μm and the diameter of each circular disk is still set to be 1.0 μm. Each of them is located in one of the four quadrants, offset from the center by 0.75 μm in both directions.

Figure 3.13 shows the simulated absorption spectra of MIM structures with the uniform circular and the uniform raindrop disk arrays. For the structure topped with the circular micron disk arrays, as the black curve shows, the peak absorption reaches 99.6% at the wavelength of 3.72 μm Meanwhile, the one containing the raindrop-shaped arrays presents two peaks with the absorption of 92.4% and 95.3% at the wavelength of 3.68 μm and 4.06 μm respectively, which is shown as the red curve in Figure 3.13.

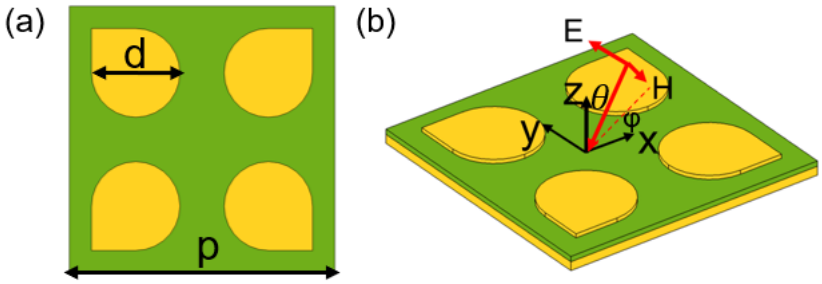

Figure 3.12: Schematic structure of the designed unit cell with raindrop shaped disk

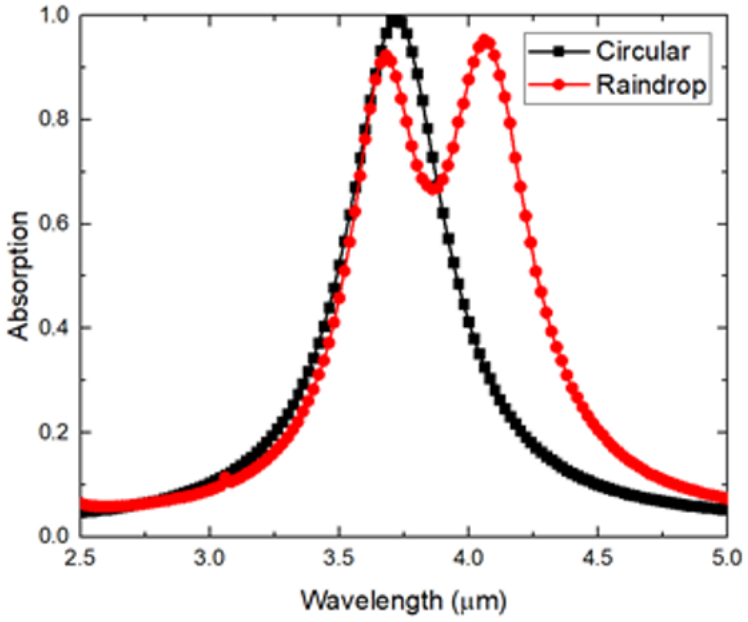

Figure 3.13: Simulated absorption spectra of circular and raindrop disk arrays.

Figure 3.14 displays the electric field $|Ey|$ and magnetic field $|Hx|$ distributions of raindrop-shaped resonator at absorption peaks of 3.68 μm and 4.06 μm As indicated in Figure 3.14(a), Figures 3.14(b) and 3.14(c) show the electric field intensity distribution $|Ey|$ at the interfaced between the metallic particle layer and the insulator spacer at the resonance wavelengths 3.68 μm and 4.06 μm, while Figures. 3.14(e) and 3.14(f) are the magnetic field intensity distributions at the two resonance wavelengths of the cross section area, indicated by Figure 3.14(d). The symmetricity changing from a circle to a raindrop shape generates the extra absorption peak in the raindrop shaped absorber. The electric field distributions $|Ey|$ of Figure 3.14(b) and 3.14(c) clearly show the excitation of electric dipole resonances at two resonant wavelengths. The magnetic field distributions $|Hx|$ of Figure 3.14(e) and 3.14(f) show the localization of magnetic field in the insulating layer which is caused by oppositely oriented current sheets on the disk and the ground plane [49].

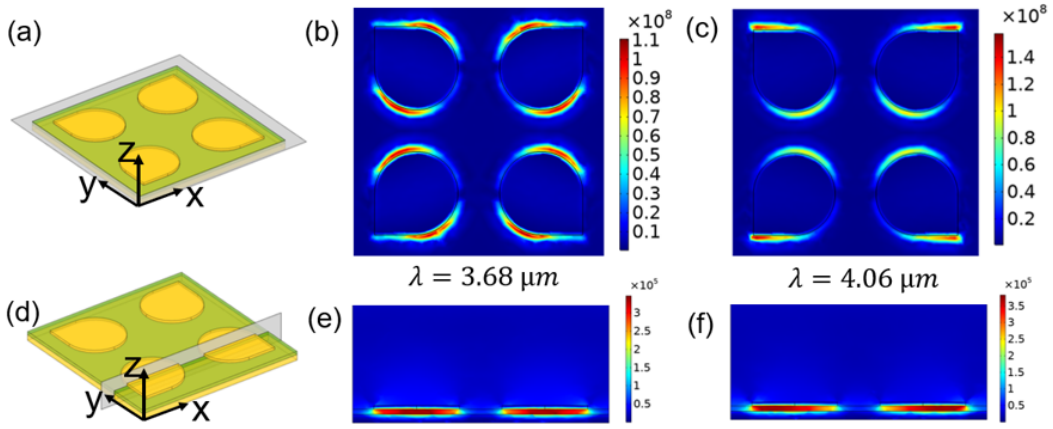

Figure 3.14: $|Ey|$ and $|Hx|$ field distributions at absorption peaks of 3.68 μm and 4.06 μm.

As shown in Figure 3.15(a), the sizes effect on the absorption spectra of the raindrop shape absorber is studied. It shows a tunable range of two resonant wavelengths with a fixed size of period p. Increasing the size d of the raindrop shape disk results a red shift of the absorption peaks. For d = 1000 nm, two absorption peaks are achieved at resonant wavelengths of 3.68 and 4.06 μm. The two absorption peaks shift to lower wavelengths of 3.02 and 3.34 μm for the case of d = 0.8 μm. The smaller size of the

raindrop shape disk can result in a lower capacitance of the structure. Figure 3.15(b) shows the absorption spectra with different thickness of dielectric layer. It can be seen that the peak absorptions can be shifted to smaller resonant wavelengths by increasing the thickness of the dielectric layer. The increase of the thickness of the dielectric layer can result in a blue shift of the resonances and the optimization of the absorption. When the thickness of the dielectric layer reaches 90 nm, the two peak absorptions can exceed 99.9%. With the increase of the dielectric layer, or the decrease of the raindrop shape disk size, the capacitance of the resonator decreases which results the resonant frequency $w = 1/\sqrt{LC}$ increases, corresponding to the decrease of the wavelength, where L and C are the inductance and capacitance of the structure respectively [49].

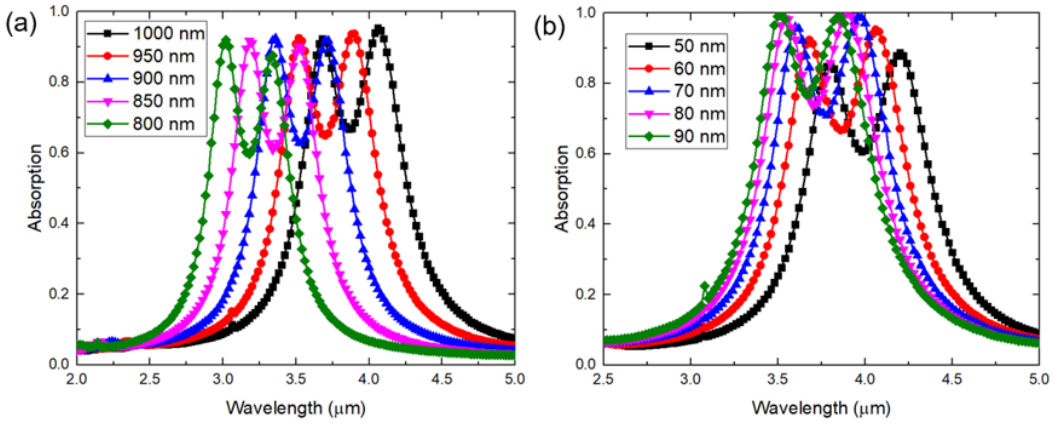

Figure 3.15: Absorption spectra with (a) varied sizes d of raindrop shape, and (b) varied thickness of dielectric layer.

The absorption spectra of the varied incident and azimuthal angles are displayed in Figure 3.16. Two absorption peaks indicated by two red strips remains high absorption under TE polarization for the incident angles θ up to 30 degrees. And the position of the two absorption peaks is still maintained. Due to its four-fold symmetricity, the structure is not sensitive to polarizations. As shown in Figure 3.16(b), the absorption peaks remain the same with different azimuthal angles under normal incidence.

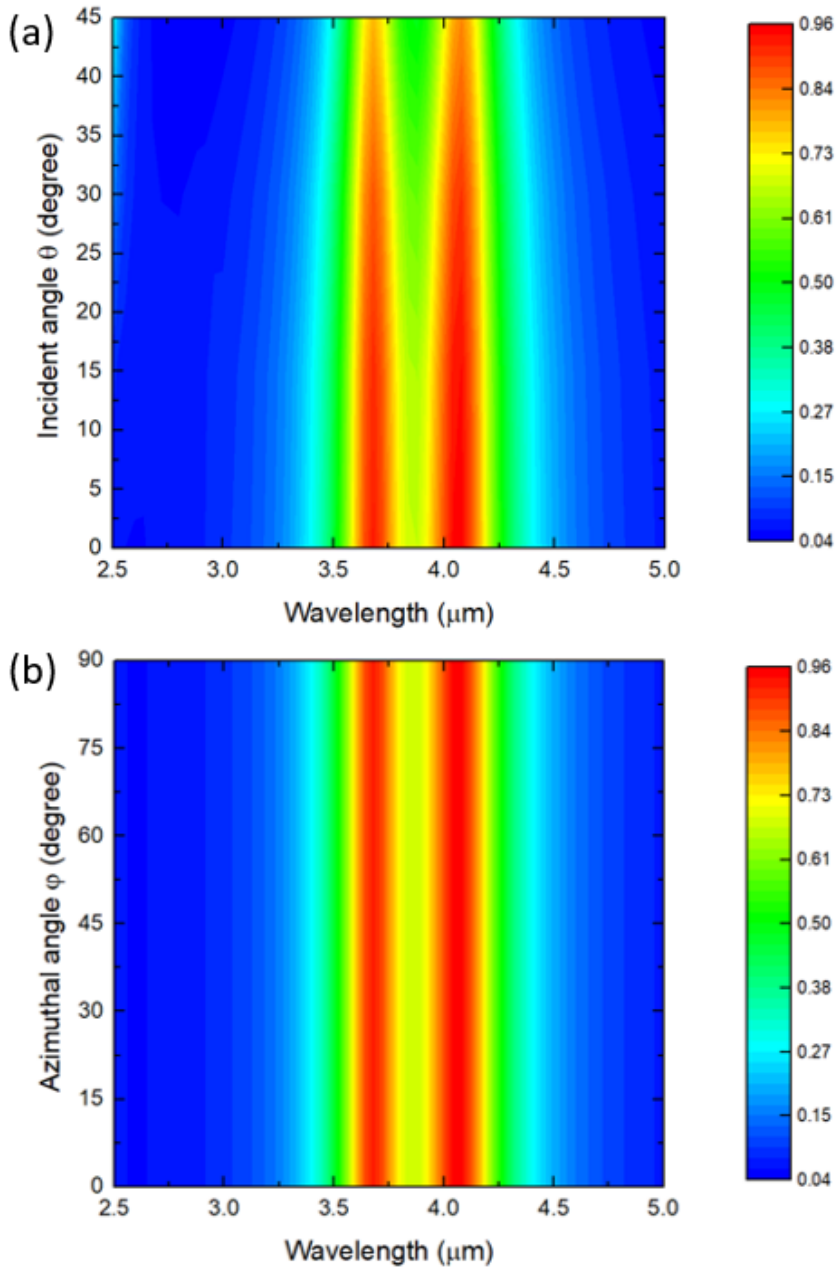

Figure 3.16: (a) Absorption spectra with varied incident angles θ while azimuthal angle $\phi = 0°$. (b) Absorption spectra with varied azimuthal angles θ under normal incidence.

3.4 Design of a broadband metamaterial absorber

Due to the fact that each shape of resonator can generate resonance at specific wavelength, a broadband absorption can be achieved by combining two different shapes into one unit cell. Figure 3.17 shows the schematic unit cell of the combined resonators. The whole top metallic layer is formed by aligning these unit cells periodically and adjacently. In each unit cell, the raindrop shaped disks with different sizes d = 1.0 μm and d1 = 0.80 μm are each located in one of the four quadrants, offset from the center by 0.75 μm in both directions, as shown in Figure 3.17. In order to achieve the maximum absorption, the thickness of dielectric layer SiO_2 is modified to 0.18 μm while the thicknesses of the top gold raindrop arrays and the ground plane stay the same.

As shown in Figure 3.17, all the raindrop shape disk point to the same direction. The structure can achieve the highest absorption when the azimuthal angle is zero degree with normal incidence under TE case. However, the absorption intensity greatly decreases when the azimuthal angle is 45°.

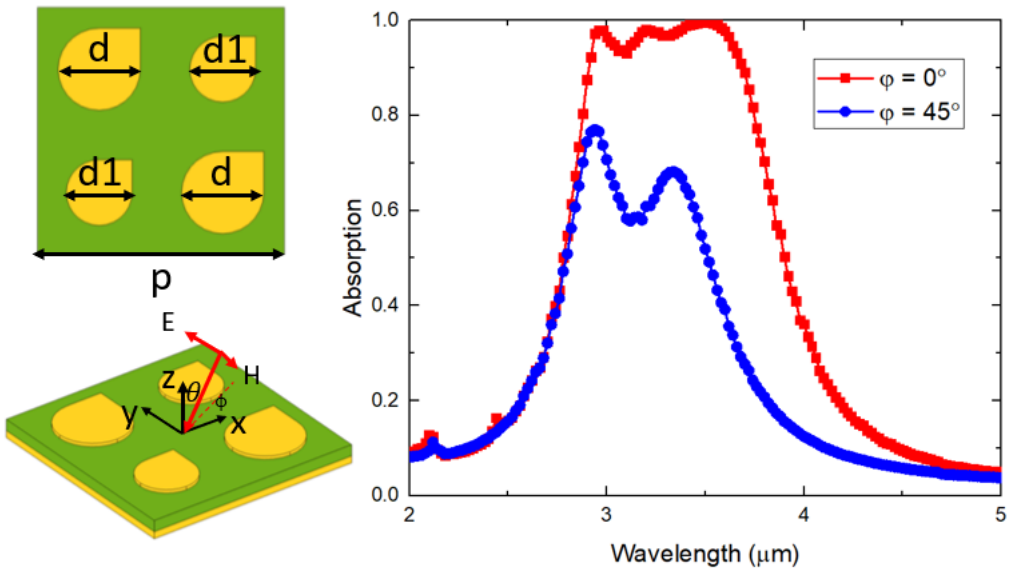

Figure 3.17: Schematic unit cell with resonators pointing in same direction.

As shown in Figure 3.18, the raindrop shape disks with same size is set to be along the same diagonal line. As the blue curve indicates, the absorption intensity is greatly

reduced when the azimuthal angle is 45°.

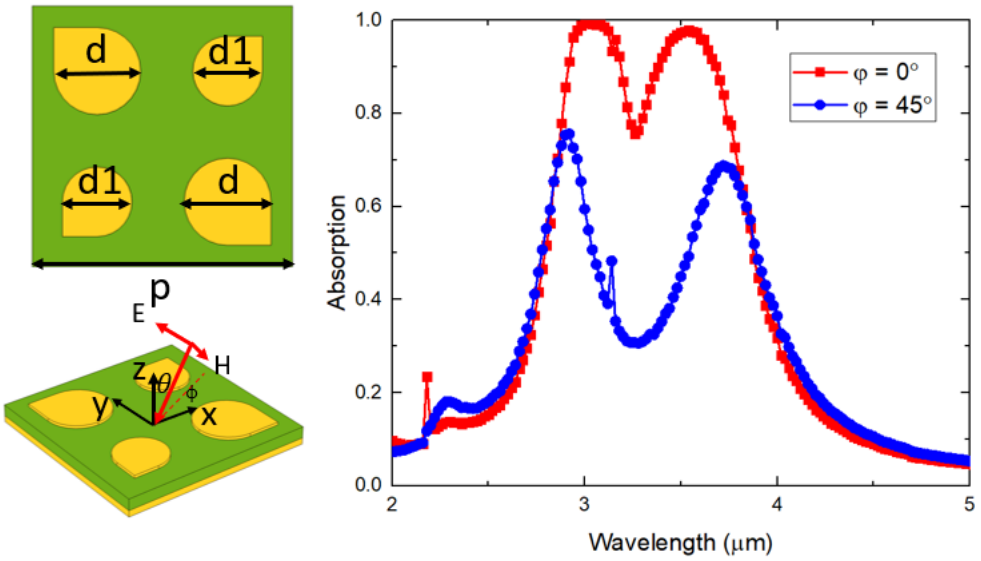

Figure 3.18: Schematic unit cell with same sized resonators aligned diagonally

Among the four raindrops in each unit cell, the two horizontal ones are sized differently while the two vertical ones are the same, as shown in Figure 3.19. The difference between this configuration and previous two configurations is that raindrop shape disks with same size can be overlapped by rotating 90° along the center of the unit cell.

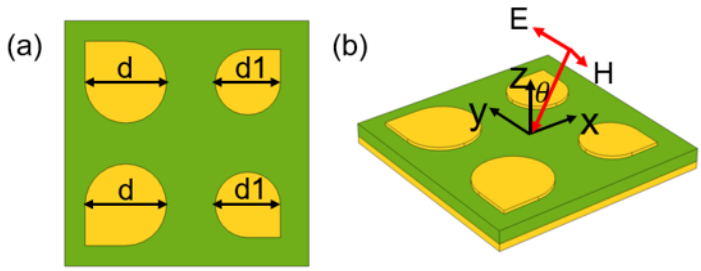

Figure 3.19: Schematic unit cell with same sized resonators aligned vertically

From Figure 3.20, it can be seen that a wider absorption band is achieved by multiplexing two different sizes of raindrop disks into one unit cell. As displayed by Figure 3.20, even the structure is not four-fold symmetric, it still remains wide absorption for

different azimuthal angles. As shown in Figure 3.21, the structure maintains high absorption for the incident angles up to 30°. The absorption wavelength from 2.80 μm to 3.90 μm is covered with absorption higher than 50%.

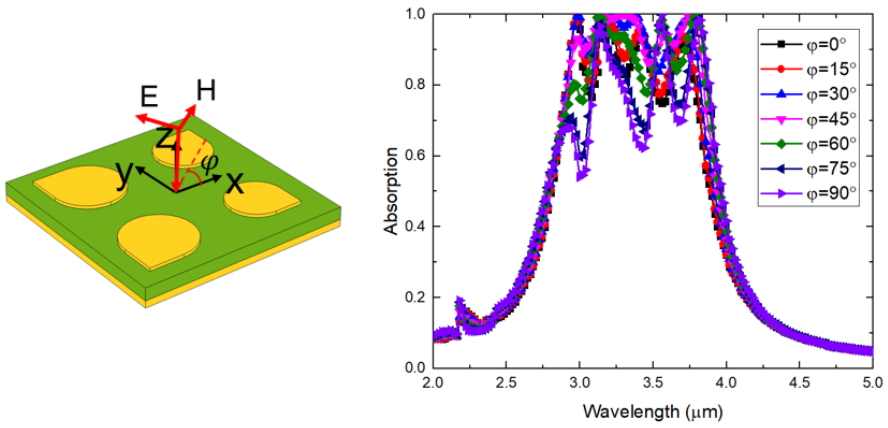

Figure 3.20: Absorption spectra with different azimuthal angles ϕ under normal incidence.

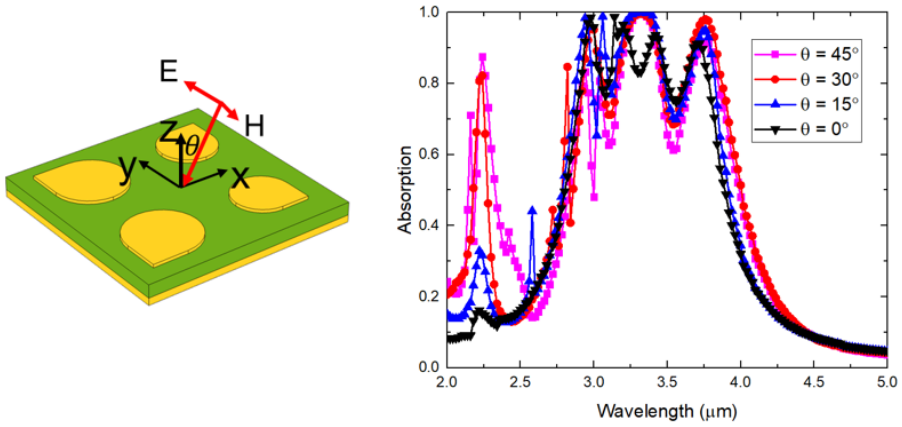

Figure 3.21: Absorption spectra with different incident angles θ while azimuthal angle $\phi = 0°$.

3.5 Conclusion

In conclusion, resonators with different shapes can generate different resonant wavelength. Broadband metamaterials absorbers topped with on raindrop shaped submicron disks have been theoretically investigated. Compared to circular disk absorber, the uniform raindrop shaped absorber can achieve two absorption peaks with wider absorption bandwidth. Furthermore, by breaking the uniform arrangement of the raindrop disks and setting those disks with two different sizes, it turned out that the absorption spectrum could be further broadened. The absorber with two different sizes raindrop shaped disks multiplexed can achieve absorption above 50% at band ranges from 2.8 μm to 3.9 μm.

Chapter 4

Experimental Realization

4.1 Introduction

The previous chapter described the proposed metamaterial absorbers by using computational modeling and simulation method. Compared to uniform circular disk that possesses only one absorption peak, the uniform raindrop shaped disk can achieve a broadband absorption. By combining two different sizes raindrop shaped resonantors into one unit cell, an even broader absorption band can be achieved.

In this chapter, we demonstrate a metamaterial fabrication process based on E-beam lithography method. The proposed metamaterial absorber devices were fabricated by E-beam lithography, imaged by Scanning electron microscopy (SEM) and the absorption of the devices were measured by Fourier Transform Infrared Spectroscope.

4.2 Fabrication of proposed absorbers

E-beam lithography method can have high control over the resonator's size and shape, and is widely used to fabricate infrared metamaterial absorbers [30]. The absorbers with varied shapes proposed in previous chapter are fabricated and measured, as shown in Figure 4.1.

Figure 4.2 shows the E-beam lithography fabrication process of the metamaterial absorber device. The fabrication size for each pattern is 0.5 mm x 0.5 mm. There are six steps in general which are described in details as following.

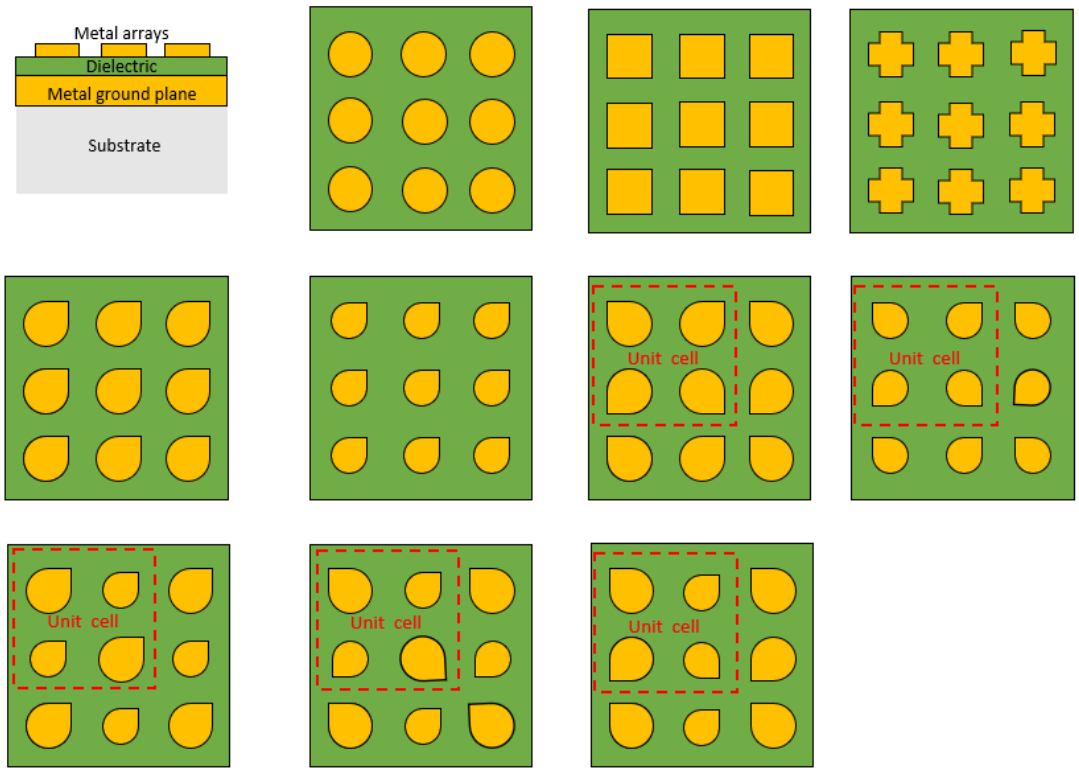

Figure 4.1: Schematic of metamaterial absorber structures

First step: A thickness of 10 nm Ti layer was deposited on a clean silicon wafer by using the AJA2 sputtering system for adhesion layer. Then gold with thickness 100 nm and SiO_2 with thickness 60nm were deposited on the Ti layer. The AJA2 sputter system sputters materials from source targets to substrates utilizing ionized gas (Ar, O_2, N_2) , and it is an very effective physical vapor deposition technician for depositing thin films. There are six shuttered guns on the system: 3 RF (Radio Frequency), and 3 DC. DC sputtering used DC volts and is mainly used when deposing conductive materials. While RF power is AC and can be used for both conductive and non-conductive materials. During sputtering process, RF guns were used for depositing Ti and SiO_2 layer, and DC gun was used to deposit gold. Because gold can not stick on the surface of silicon wafer very well, the adhesion layer Ti is needed here. For Ti deposition, 50 sccm Ar flow was used and the pressure is set to be 5 mTorr. The deposition rate was 7 nm/min, and

86 seconds were used. We deposited SiO_2 for 5538 seconds with 0.65 nm/min deposit rate under 5 mTorr pressure, 48 sccm Ar flow and 2 sccm O_2 flower. Finally, 10 nm thickness Ti layer, 100 nm gold layer and 60 nm thickness SiO_2 layer were achieved.

Second step: Poly(methyl methacrylate) (PMMA) was used as an E-beam positive resist. PMMA C2 was spun on a spin coater at 1500 rmp for 30s, which roughly deposited a 150 nm thickness resist thin film. Then, the sample was baked on a hot plate for 120s at 180°.

Third step: The desired patterns created by Clewin5 were exposed to the PMMA layer by E-beam lithography. The model name of the E-beam machine used in this process is Vistec EBPG5000+ system. The dose current was set to be 1200 $\mu C/cm_2$ at 100 kV.

Fourth step: After E-beam lithography, the sample was removed from the E-beam machine and developed in 3: 1 isopropanol : methyl isobuty1 ketone (IPA:MIBK) solution for 40 s. Then the sample was rinsed in pure IPA solution and dried in nitrogen stream from a nitrogen gun. After the development, the areas exposed to electron beam were removed.

Fifth step: A 5 nm thin Ti layer and a thickness of 45 nm gold layer were deposited on the sample by E-beam evaporation in CHA E-beam evaporator system.

Sixth step: A lift-off process was performed after we removed the sample from the CHA evaporator once the gold layer is deposited.The sample was dipping in N-Methy-2-Pyrrolidinone (NMP) for 20 minutes at 90°. So the remaining PMMA layer on the top can be removed.

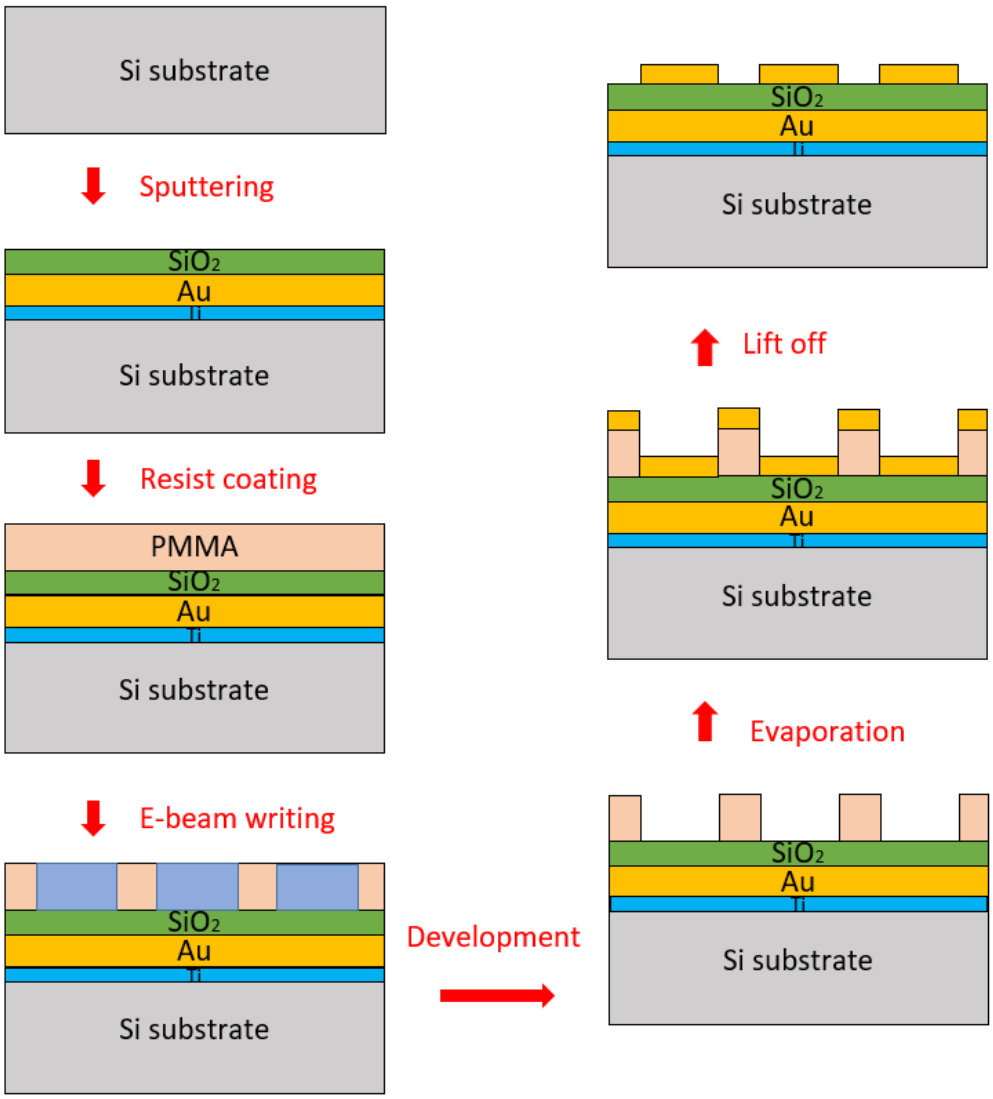

Figure 4.2: MA fabrication process based on E-beam lithography method

4.3 Scanning electron microscopy

SEM was used to characterize the fabrication results of the structure. Figures 4.3, 4.4, and 4.5 shows the SEM images of the fabricated devices. In the measurement, top views of the structure from SEM were recorded. The circular, square and cross disks patterns are shown in Figure 4.3. The raindrop shaped absorbers with same size in each unit cell are shown in Figure 4.4, while Figure 4.5 displays the the raindrop shape absorber with different sizes in each unit cell and different configurations.

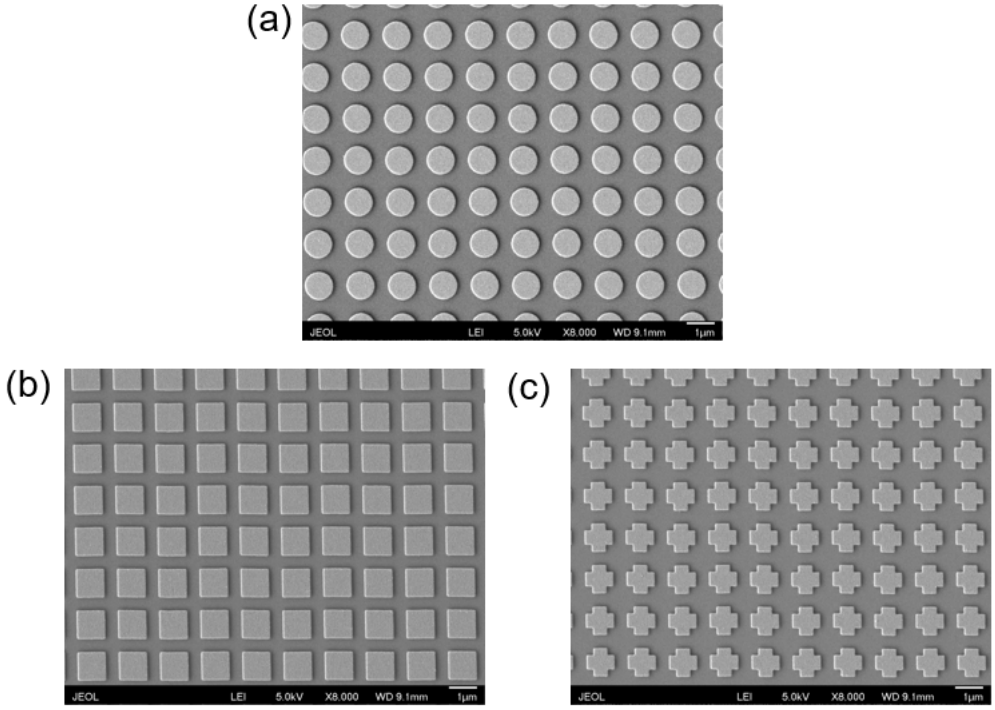

Figure 4.3: SEM images of the fabricated devices: (a) circular, (b) square, (c) cross disks.

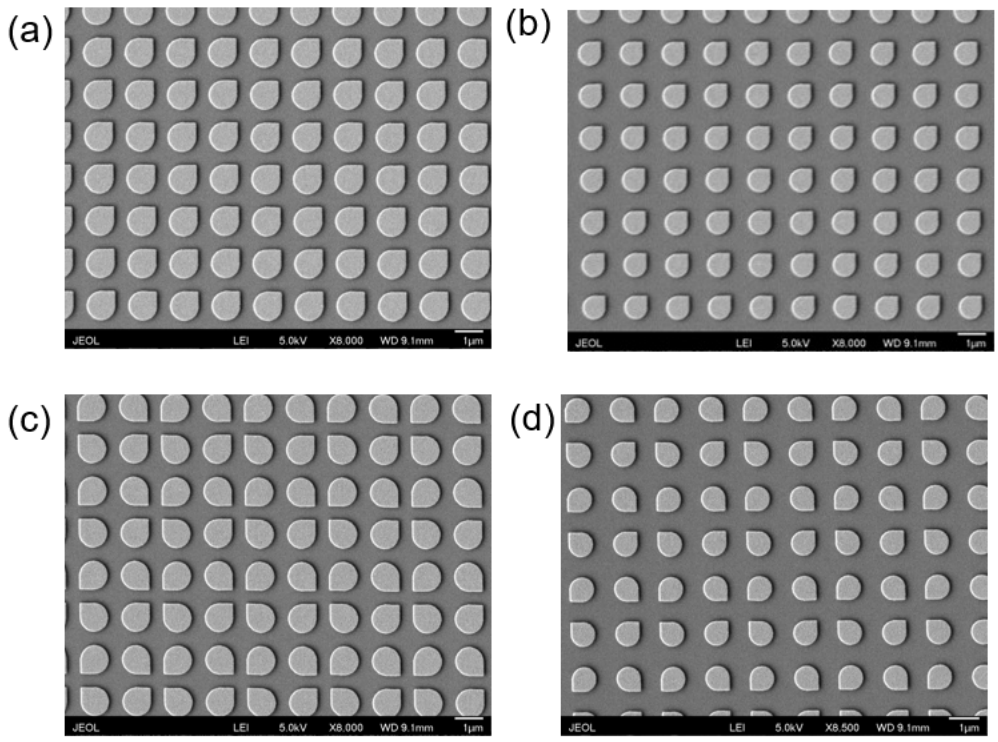

Figure 4.4: SEM images of the fabricated raindrop shape absorbers with same size in each patterns and different configurations (a) 1.0 μm, (b) 0.8 μm, (c) 1.0 μm, (d) 0.8 μm.

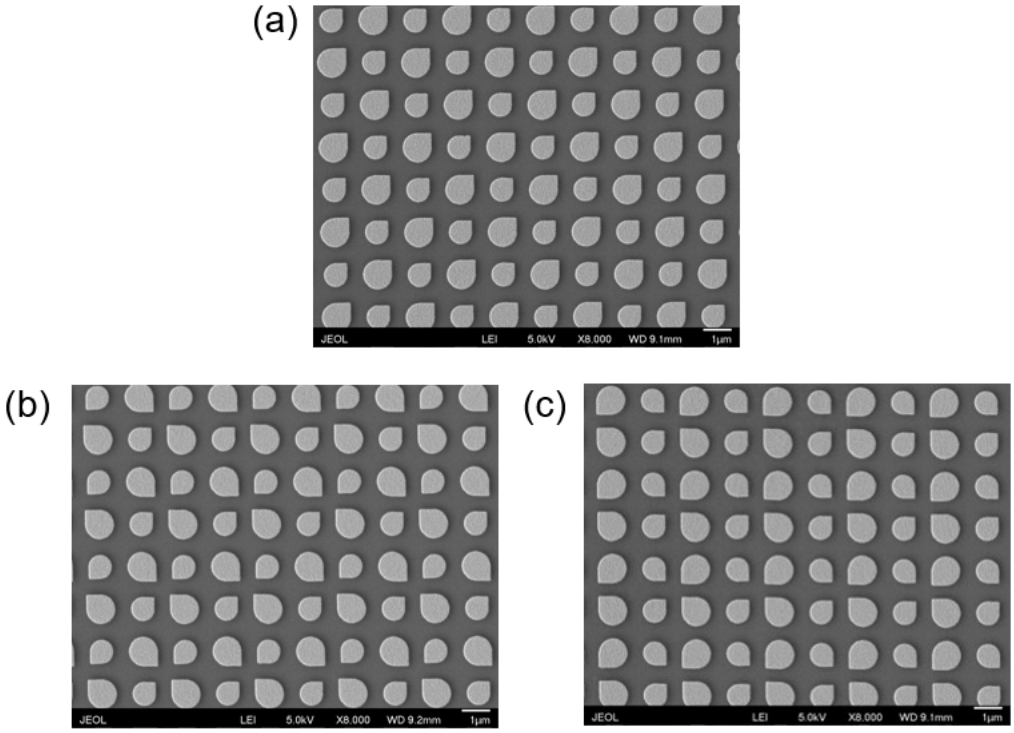

Figure 4.5: SEM images of the fabricated raindrop shape absorbers with two different sizes (1.0 μm and 0.8 μm)in each patterns and different configurations.

4.4 FTIR Measurement

The reflection spectra of the absorbers were measured using a microscope coupled with a Thermo Scientific Nicolet iS50 Fourier-Transform Infrared (FTIR) spectrometer. The reflected light was collected by an IR microscope objective from a focusing area of 150 μm x 150 μm. To obtain the reflection results from the FTIR spectrometer, the background reflection from a clean planar gold surface was measured for calibration. Then the measured reflections in percentage from the absorbers were calibrated based on the background reflection.

From Figure 4.6, it can be seen that the simulation results match the experimental results well. Different shapes of resonators can generate the different resonant wavelength. The simulated absorption peaks for circular, square and cross shapes are 3.72, 4.38 and 3.90 μm respectively, while the experiment test results show the corresponding absorption peaks are located at 3.74 μm, 4.36 μm and 3.88 μm. Due to its four-fold symmetry property, the structure is not sensitive to the polarization of the incident waves [50].

As the SEM images shown in Figure 4.4(a) and (b), raindrop shape resonator pointing in the same direction has only one line of symmetry, which makes the structure sensitive to the azimuthal angles. From Figure 4.7, the FTIR test results show that the absorption intensity is greatly decreased due to its low symmetry property. The red curve shown in the Figure 4.4 is the simulated absorption spectra under TE case with polarization along y direction. However, as we decrese the diameter size of the raindrop shape from 1.0 μm to 0.8 μm, the resonant wavelengths shift to lower wavelength. The reason of this is explained in the previous chapter. As shown in Figure 4.7, when the symmetry of the pattern in each unit cell is increased, the absorption intensity is increased. As shown in Figure 4.4(c) and (d), the pattern in each unit cell is four-fold symmetry, so the structure is not sensitive to the polarization of the incident waves. From Figure 4.7(c), two absorption peaks are observed at wavelengths 3.75 μm and 4.10 μm from FTIR test, respectively, which is slightly different from the simulated absorption spectrum. The minor difference between experimental and theoretical results can be attributed to the fabrication imperfections.

As shown in Figures 4.8(a) and (b), the structures which are sensitive to azimuthal

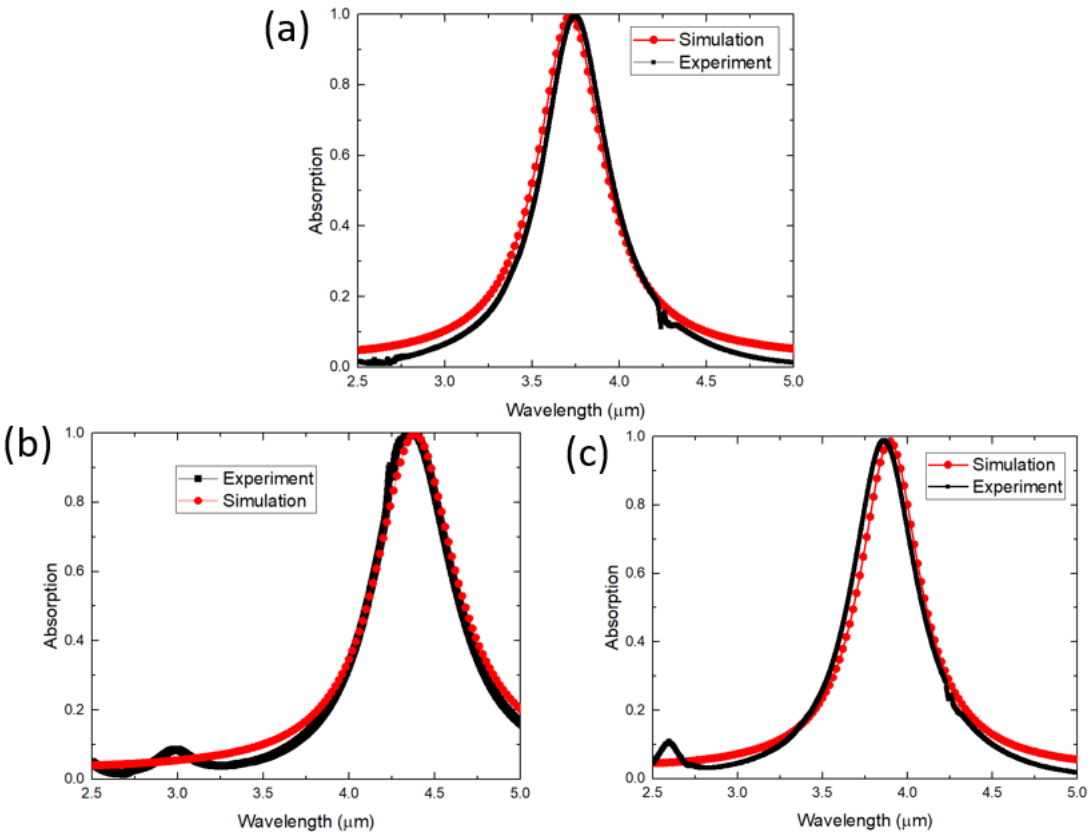

Figure 4.6: FTIR test results of different shape resonators: (a) circular disk, (b) square disk, (c) cross disk corresponding to Figure 4.3.

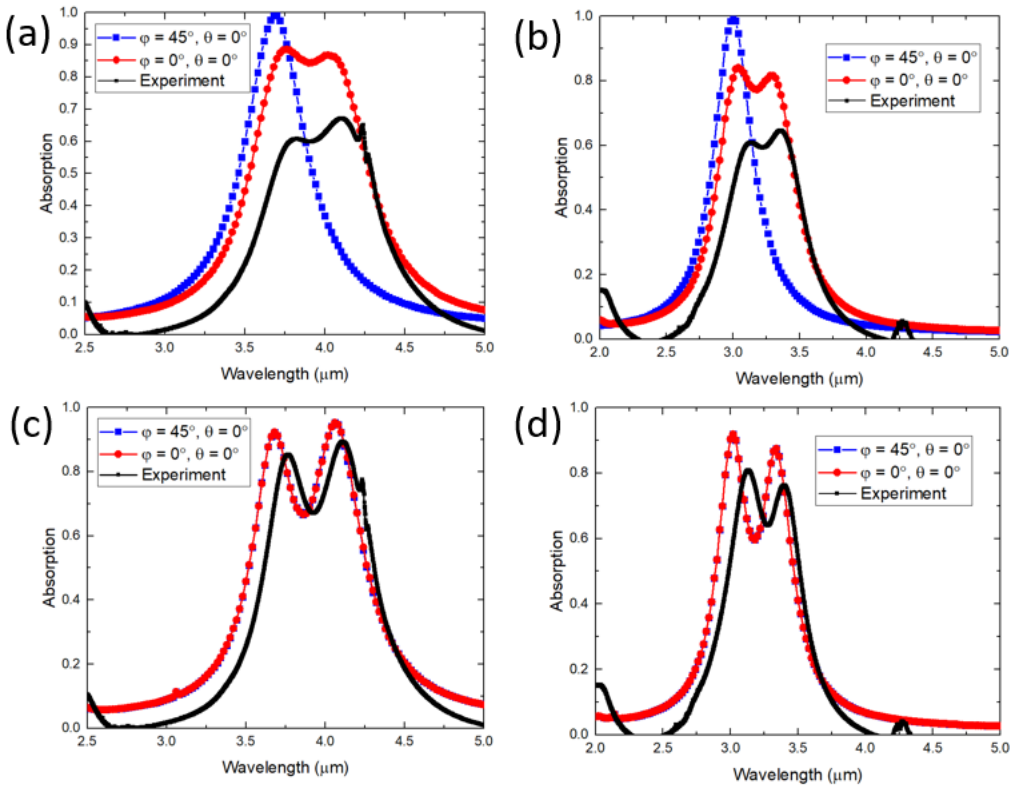

Figure 4.7: FTIR test results of the raindrop disks with same size in each pattern corresponding to Figure 4.4.

angles of the incident waves have low absorption intensity. As indicated by Figure 4.8, a wider absorption band is achieved in the wavelength range between 2.70 μm and 3.82 μm with absorption level above 50%.

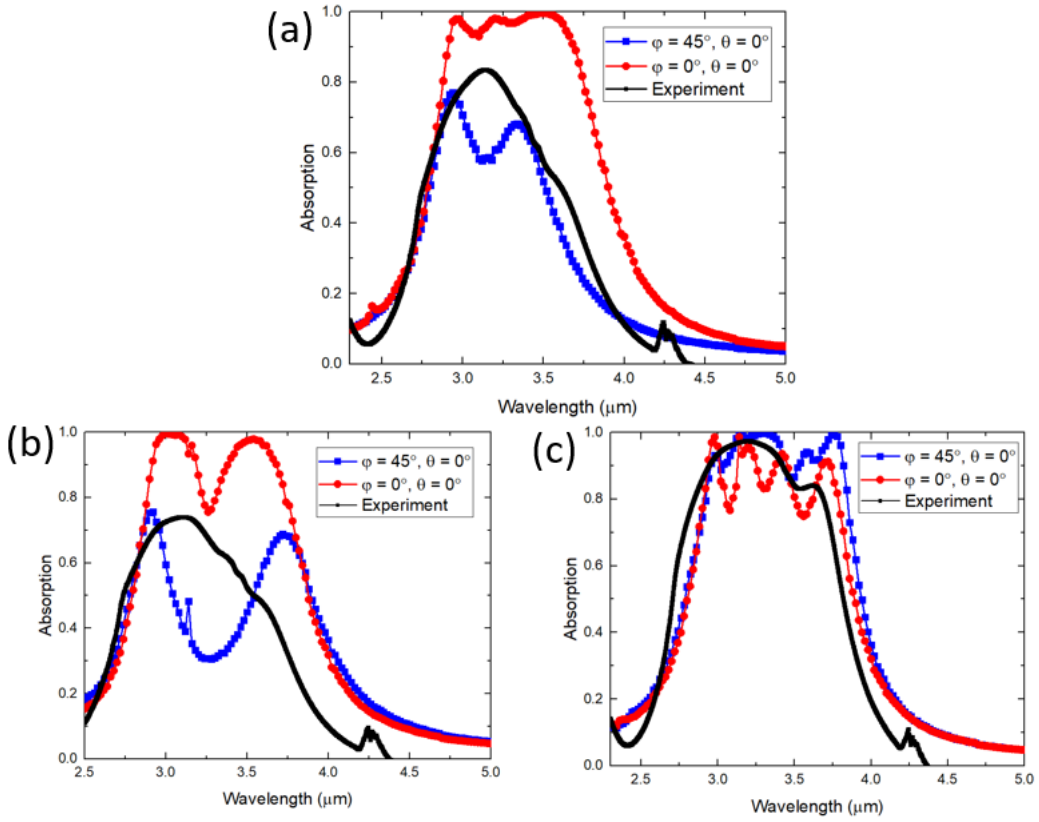

Figure 4.8: FTIR test results of the raindrop disks with two different sizes in each pattern corresponding to Figure 4.5.

Except the structure symmetry effect on the absorption spectra, the difference between simulation and experiment results can be raised from fabrication errors, which includes the slight inaccuracy of the thickness of SiO_2 layer during sputtering process and the slight inaccuracy of shape size during E-beam lithography process. In general, the broadband absorption can be achieved by the MIM based metamaterial absorbers with raindrop shaped disks on the top layer.

4.5 Conclusion

In this chapter, details of the E-beam fabrication process of the proposed absorbers are presented and the FTIR test results are analysed. Overall, our experimental results confirm that the broadband absorption can be achieved by the MIM based metamaterial absorbers with raindrop shaped disks on the top layer.

Chapter 5

Design of a multi-band metamaterial absorber

In this chapter, a five-band terahertz metamaterial absorber with a novel structure is described and analyzed. This structure consists of a cross and four quarter-sectional circular rings surrounded by a square ring within the top layer, a metallic ground plane and a dielectric middle layer. Due to its four-fold symmetric property, the structure is insensitive to the incident wave polarizations. Simulation results have revealed that the absorber possesses five distinct absorption peaks at 0.7, 1.6, 2.32, 2.63, and 3.15 THz frequencies, with an average absorptivity exceeding 96.7%. In this work, the electric field intensity is simulated to reveal the resonance mechanism of the five-band absorber.

5.1 Absorber Structure Design

Figure 5.1 shows the proposed five-band absorber structure, only one unit cell is shown here. It consists of three functional layers, namely gold arrays on the top, gold ground plane, and a dielectric layer between the two metal layers, with respective thicknesses of 0.5 μm, 10 μm, and 2 μm. Polyimide with a dielectric constant $\varepsilon = \varepsilon_0 (1 + i\alpha) = 3(1 + i0.06)$ [51] is chosen for the middle dielectric spacing layer, while the conductivity of gold is 4.09×10^7 S/m.

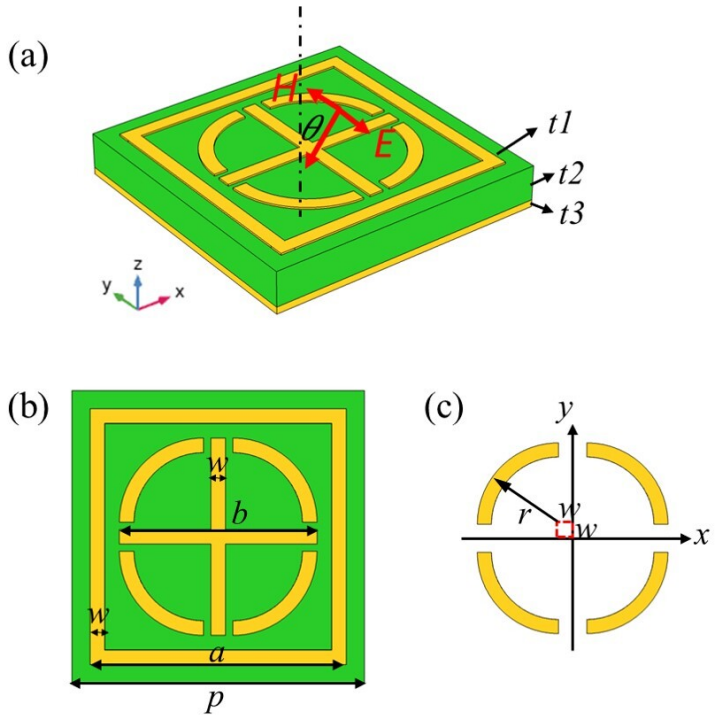

Figure 5.1: Absorber unit cell structure with p = 80, a = 70, b = 54, r = 23, and w = 4 (all dimensions are given in μm): (a) the perspective view, (b) the top view, and (c) four quarter-sectional circular rings.

The electromagnetic responses of the absorber were simulated by utilizing the commercial finite element software COMSOL Multiphysics. In simulations, periodic boundary conditions were performed in x and y directions, and in the z direction, perfectly matched layer conditions were applied. The absorptivity of the structure was calculated by adopting the following expression [41]:

$$A(\omega) = 1 - R(\omega) - T(\omega) = 1 - S_{11}^2 - S_{21}^2 \tag{5.1}$$

where A, R, and T represent the absorption, reflection, and transmission of the absorber, respectively, and S_{11} and S_{21} denote the reflection and transmission coefficient. The metallic gold ground plane on the bottom is thicker than the skin depth of the frequency at 3.5 THz, preventing the transmission of the EM waves, so the transmission through the structure is negligible. Consequently, the absorption through the proposed structure can be expressed as $A(\omega) = 1 - R(\omega) = 1 - S_{11}^2$. Unity absorption can be achieved

when the impedance of the structure is identical to free space [1, 52].

5.2 Electrical Field Distribution Analysis

The absorption spectra of the absorber developed as a part of the present study, shown in Figure 5.2, indicates that the designed absorber produces five distinctive absorption peaks at 0.7, 1.6, 2.32, 2.63, and 3.15 THz with the corresponding absorption rates of 98.4%, 99.6%, 93.8%, 94.2%, and 97.7%, respectively. The absorber loss mechanisms were further studied in order to identify the physical origins of the characteristics demonstrated by the absorber.

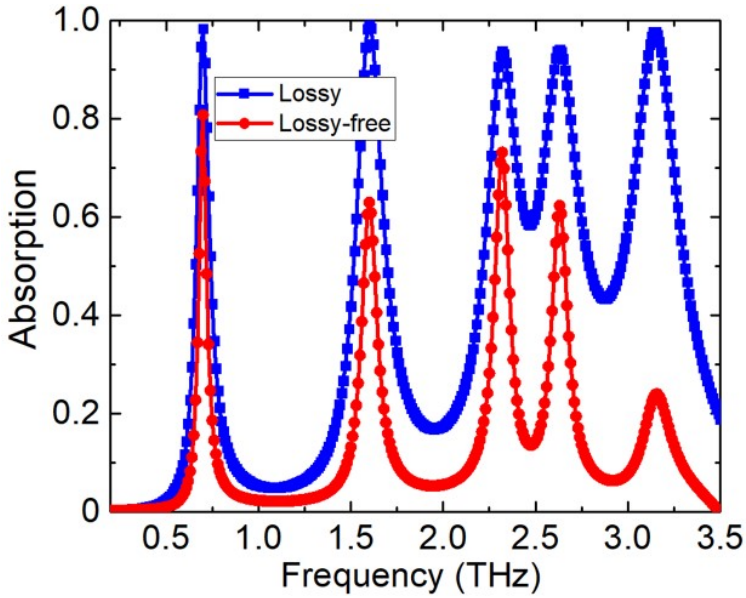

Figure 5.2: Absorption spectra of the absorber with loss-producing and loss-free dielectric layer.

Figure 5.2 displays the absorption spectra of the loss-producing and loss-free dielectric layer at constant metal layer conductivity. In Figure 5.2, when the imaginary part of the dielectric layer is equal to zero (i.e. loss-free), as displayed by the red line, the height of the peaks declines while their positions remain unchanged, which is consistent with the findings reported by other authors [53]. Moreover, while at the fifth peak the energy is consumed as dielectric loss, the dissipation related to the remaining peaks is

due to dielectric and ohmic losses.

The absorption spectra pertaining to the transverse electric (TE) and transverse magnetic (TM) polarization are shown in Figure 5.3. Due to the four-fold symmetric property, the symmetric absorber is not sensitive to TE and TM polarizations [54], concluded by the identical pertinent absorption spectra.

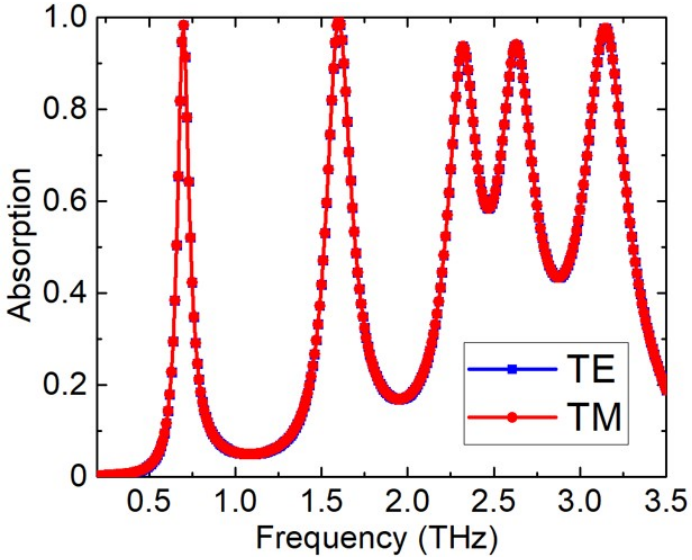

Figure 5.3: Absorption spectra of the absorber at TE and TM.

Figures 5.4 and 5.5 display the electric field ($|E|$ and real (E_z)) distributions for the designed absorber at the previously identified five absorption peaks (0.7, 1.6, 2.32, 2.63, and 3.15 THz), which are labeled as modes f1, f2, f3, f4, and f5, respectively.

In mode f1, as can be seen in Figure 5.4(a), the electric field $|E|$ is particularly concentrated on the left and right baselines of the square ring structure, indicating that large charges are accumulated in these regions [55], as confirmed by the electric field E_z distributions shown in Figures 5.5(a1) and 5.5(a2). Similarly, Figure 5.5(a1) indicates that, opposite charges accumulate on the left and right baselines of the square ring structure, confirming the electric dipole resonance in the square ring metallic structure. Moreover, in mode f2, electric fields are accumulated on the left and right side of the cross shape, as displayed in Figure 5.4(b). Additionally, Figures 5.5(b1) and 5.5(b2) show the excitation of the electric dipole resonance in the cross shape at the frequency of 1.6 THz because of the opposite charges. In Figures 5.4(c) and 5.4(d), electric fields

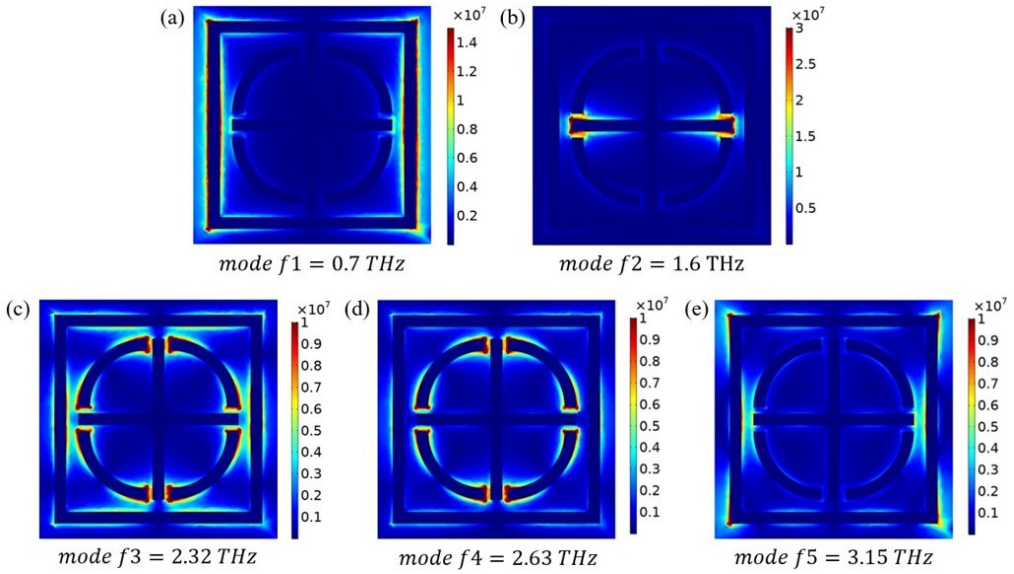

Figure 5.4: Electric field $|E|$ distribution at the interface of the top gold layer and the dielectric layer for the designed absorber at different frequencies in THz (a) f1 = 0.7, (b) f2 = 1.6, (c) f3 = 2.32, (d) f4 = 2.63, and (e) f5 = 3.15.

develop on the edges of not only the four quarter-sectional circular ring structures, but also on the square ring structure. From Figure 5.5(c1), it is obvious that opposite charges are concentrated on the edges of the four quarter-circular ring structures, confirming that this resonance is attributed to the dipolar response from the four quarter-sectional circular rings. For the square ring structure in mode f3, hexapolar resonance is excited, which is shown in Figure 5.5(c2). For mode f4 at the 2.63 THz frequency, as illustrated in Figures 5.5(d1) and 5.5(d2), three dipolar pairs are induced by the positive and negative charges, due to which the electric hexapoles are generated. Hence, the high absorptions in mode f3 and f4 are attributed to the generation of high-order EM resonance. In mode f5, the induced electric fields are primarily located on the edges of the outer square ring, as shown in Figures 5.4(e). From Figures 5.5(e1) and 5.5(e2), it is clear that only one dipolar pair is generated by the positive and negative charges. Hence mode f5 can be identified as dipolar resonance where the fifth absorption peak occurs. In general, all five resonant modes discussed above produce strong electric resonances, and both dipolar and high-order EM resonances are generated due to the high absorption characterizing this novel structure.

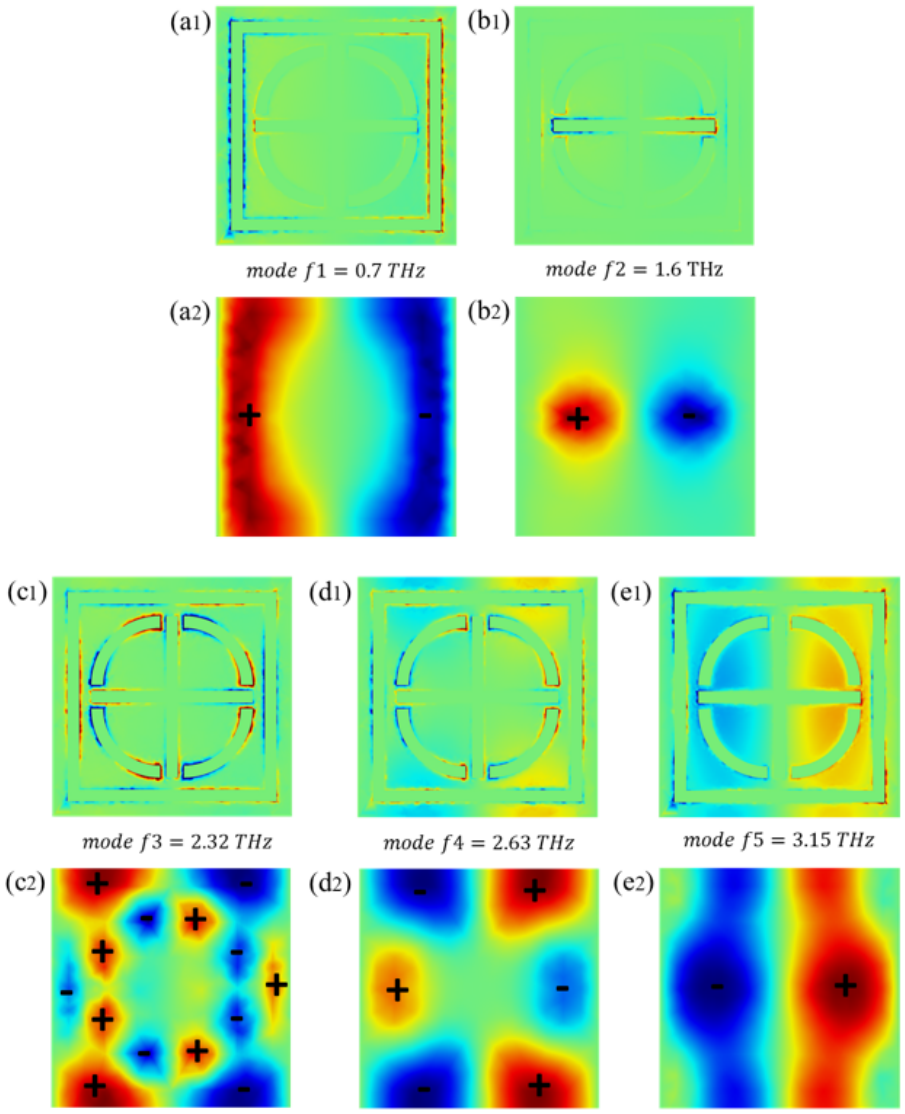

Figure 5.5: Electric field real(E_z) distribution at the interface of the top gold layer and the air layer for the designed absorber at different frequencies in THz (a1) f1 = 0.7, (b1) f2 = 1.6, (c1) f3 = 2.32, (d1) f4 = 2.63, (e1) f5 = 3.15. The electric field real(E_z) at the interface of the bottom gold layer and the dielectric layer at these same frequencies in THz is also shown: (a2) f1 = 0.7, (b2) f2 = 1.6, (c2) f3 = 2.32, (d2) f4 = 2.63, and (e2) f5 = 3.15.

5.3 Parameter changes Analysis

The effects of parameter changes on the designed absorber performance have also been investigated. The frequencies characterizing the modes f1, f4 and f5, and the absorption coefficient pertaining to mode f3, gradually decrease as the square ring length a increases, while the frequency and the absorption coefficient related to mode f2 remain unchanged, as displayed in Figure 5.6. This phenomenon corresponds to the frequency response observed in Figures 5.4 and 5.5. In Figure 5.7, the cross-length b has an obvious effect on the frequency position in mode f2. Specifically, the frequency of f2 gradually shift to higher value as the value of b decreases. In the LC circuit model, the frequency of the absorber can be expressed by the following formula [56]:

$$f_0 = \frac{1}{2\pi\sqrt{LC/2}} = \frac{c}{\pi l\sqrt{\varepsilon_r}} \sim \frac{1}{l} \tag{5.2}$$

where l denotes the metallic patch length, c represents the light speed in free space, and ε_r stands for the relative dielectric constant of the dielectric layer. The length of the metallic patch is inversely proportional to the resonance frequency. Simulation results of changes in the structural parameters agree with the formula above.

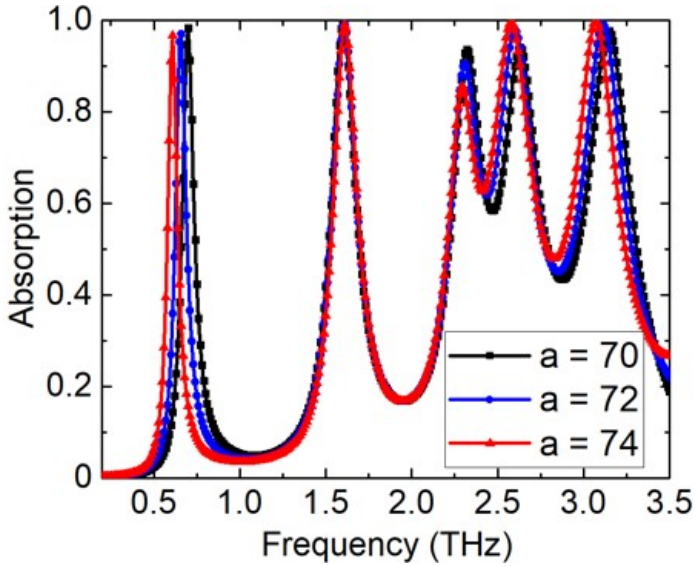

Figure 5.6: Spectra of absorption as a result of square ring length a.

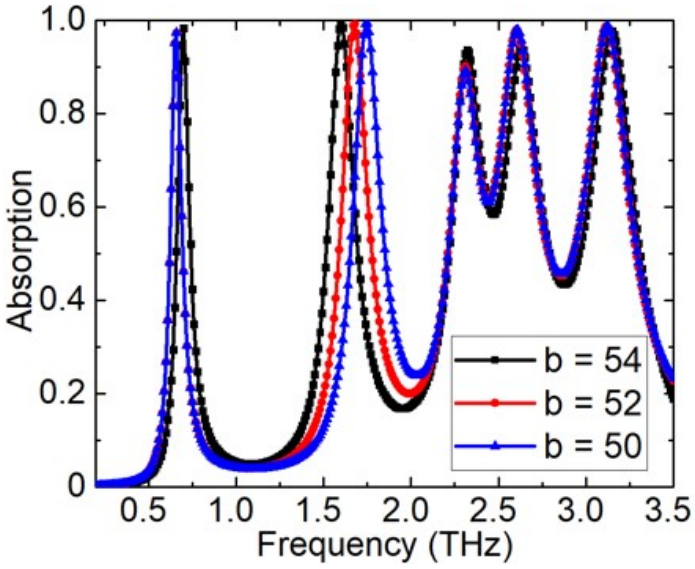

Figure 5.7: Spectra of absorption as a result of cross-length b.

From Figure 5.8, it is clear that the frequencies of modes f3 and f4 shift to higher frequency as radius r decreases while the frequency and the absorption coefficient related to mode f1, f2 and f5 remain unchanged. The change in the dielectric thickness also exerts a significant influence on the absorption frequencies. Figure 5.9 displays the effects of the thickness t2 of dielectric layer on the absorption peaks. Clearly, as t2 decreases, peak f5 shifts to a higher frequency. However, changes in t2 have limited effects on the positions of peaks of f1 to f4, while corresponding absorption coefficients decrease. In general, changing the parameters characterizing the absorber structure influences the absorption coefficients and positions of the total absorption peaks.

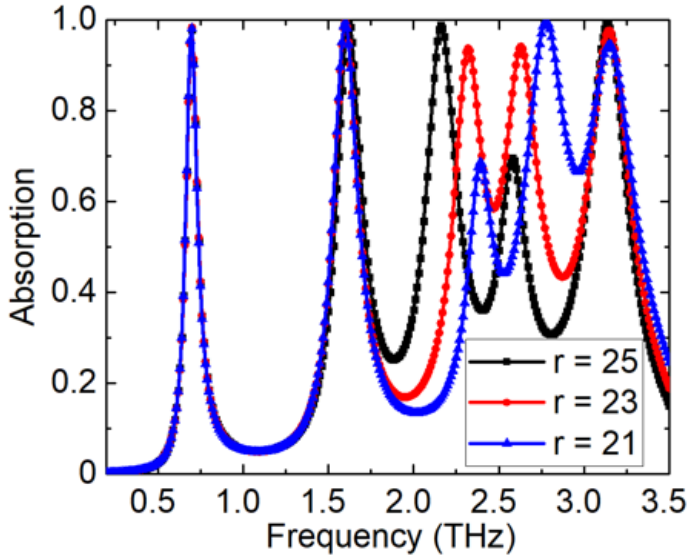

Figure 5.8: Spectra of absorption as a result of quarter-sectional circular ring radius r.

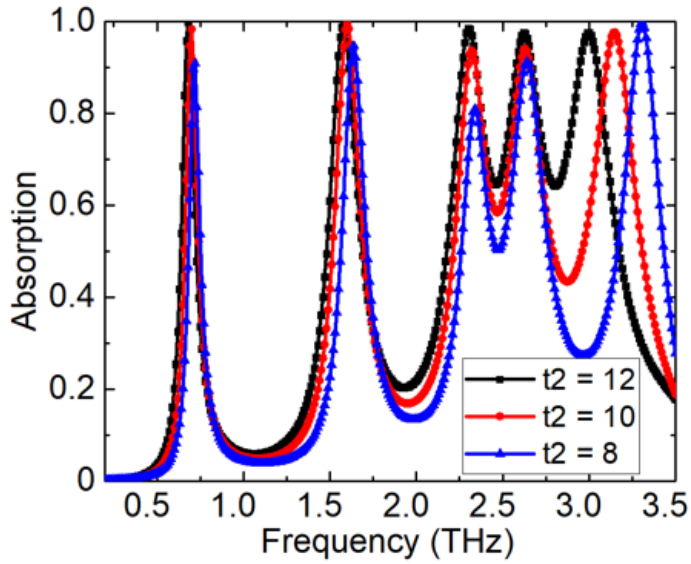

Figure 5.9: Spectra of absorption as a result of dielectric thickness $t2$.

5.4 Structural Configuration Analysis

As part of this work, we also studied the effects of structural configurations on the absorption peaks. As displayed in Figures 5.10 and 5.11, the number of total peaks can be easily adjusted through varying the structural configurations. Four absorption peaks can be produced without adding the cross structure into the design, as shown in Figure 5.10. In contrast, three strong absorption peaks emerge when a cross and square ring structures are incorporated into the design, as shown in Figure 5.11. In general, the number of the total absorption bands of this absorber can be easily altered from five to four bands, and can even to be reduced to three by varying the structural configurations.

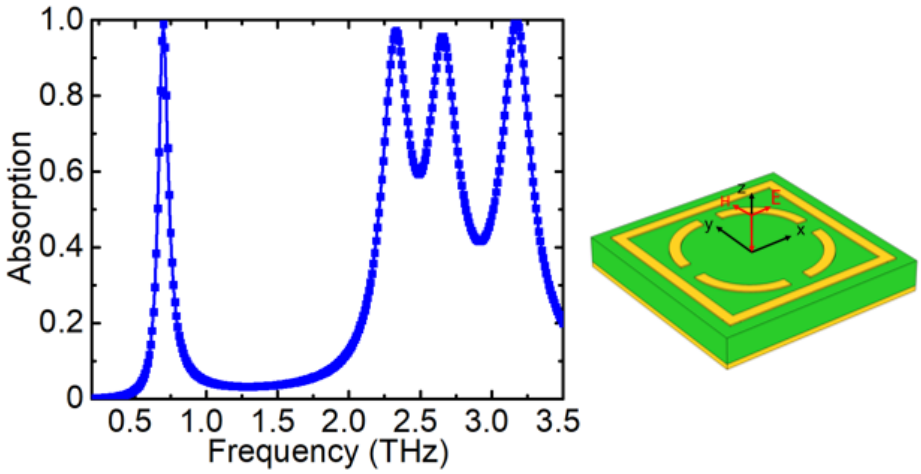

Figure 5.10: Four-band absorber with a square ring and four quarter-sectional circular rings incorporated into the structure.

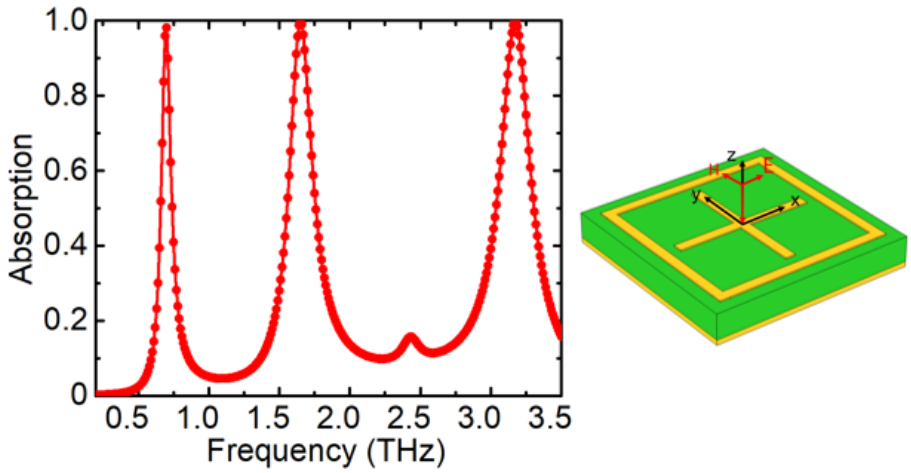

Figure 5.11: Three-band absorber with a square ring and a cross structure.

5.5 Conclusion

To summarize, a five-band terahertz absorber with high absorbance at frequencies 0.7, 1.6, 2.32, 2.63, and 3.15 THz was proposed and designed. The designed absorber is insensitive to both TE and TM polarization incident waves. The physical origins of the characteristics exhibited by this absorber can be attributed to dipolar and hexapolar resonances, as established by analyzing the electrical field density. Moreover, the influences of the main structural parameters and configurations on the absorption frequencies were studied. By varying several structural parameters, such as square ring length, dielectric thickness, and cross length, the absorption frequencies can be shifted to higher or lower values. In addition to the adjustment of absorption frequencies, the number of total resonance bands can also be adjusted by revising the structural configurations. This adjustable high-absorption five-band absorber is beneficial in a lot of engineering fields, such as detecting and terahertz imaging.

Chapter 6

Conclusion and future direction

This thesis was concerned with the design, experimental fabrication of a broadband metamaterial absorber and the design of multiple bands metamaterial absorber. The design and simulation were performed by using a commercial software COMSOL Multiphysics. The experimental fabrication were performed by E-beam lithography method. The characterization tools used were SEM and FTIR. SEM tool was used to generate images of the top view of the fabricated devices. FTIR tool was finally used to characterize the absorption spectra of the absorbers.

The structure with uniform raindrop disks could generate an additional absorption peak and consequently a much broader absorption range. Furthermore,by breaking the uniform arrangement of the raindrop disks and setting those disks with two different sizes, it turned out that the absorption spectrum could be further broadened. Experimental results confirm that the broadband absorption can be achieved by the MIM based metamaterial absorbers with raindrop shaped disks on the top layer.

Promises of THz region increases the attention on that region and researchers are trying to develop highly efficient devices that operate with THz waves. Metamaterials provide innovative solutions for overcoming the problems that have been faced with THz radiation. A flexible structure design of metamaterial absorber is also proposed in this thesis. By varying several structural parameters, such as square ring length, dielectric thickness, and cross length, the absorption frequencies can be shifted to higher or lower values. In addition to the adjustment of absorption frequencies, the number of total resonance bands can also be adjusted by revising the structural configurations. This

adjustable high-absorption five-band absorber is beneficial in a lot of engineering fields, such as detecting and terahertz imaging.

In some applications such as solar energy harvesting and photonic detection, the bandwidth of light absorbers is required to be quite broad. We proposed and demonstrated a metamaterial absorber that have broadband absorption at infrared regiem based on raindrop shaped disks. However, in the future, a broadband metamaterial absorber with high absorption efficiency in the visible light regime should be designed.

References

[1] N. I. Landy, S. Sajuyigbe, J. J. Mock, D. R. Smith, and W. J. Padilla. Perfect metamaterial absorber. *Phys. Rev. Lett.*, 100:207402, May 2008.

[2] Hu Tao, Nathan I. Landy, Christopher M. Bingham, Xin Zhang, Richard D. Averitt, and Willie J. Padilla. A metamaterial absorber for the terahertz regime: Design, fabrication and characterization. *Opt. Express*, 16(10):7181–7188, May 2008.

[3] Hu Tao, Chris Bingham, D.V. Pilon, Kebin Fan, Andrew Strikwerda, David Shrekenhamer, Willie Padilla, Xin Zhang, and Richard Averitt. A dual band terahertz metamaterial absorber. *Journal of Physics D: Applied Physics*, 43:225102, 05 2010.

[4] Yong Ma, Qin Chen, James Grant, Shimul C. Saha, A. Khalid, and David R. S. Cumming. A terahertz polarization insensitive dual band metamaterial absorber. *Opt. Lett.*, 36(6):945–947, Mar 2011.

[5] Abul Azad, Wilton Kort-Kamp, Milan Sykora, Nina Weisse-Bernstein, Ting Luk, Antoinette Taylor, Diego Dalvit, and Hou-Tong Chen. Metasurface broadband solar absorber. *Scientific Reports*, 6, 09 2015.

[6] Yanxia Cui, Kin Hung Fung, Jun Xu, Hyungjin Ma, yi jin, Sailing He, and Nicholas Fang. Ultrabroadband light absorption by a sawtooth anisotropic metamaterial slab. *Nano letters*, 12:1443–7, 02 2012.

[7] Md. Shahidul Alam, Norbahiah Misran, and Mohammad Islam. Development of electromagnetic band gap structures in the perspective of microstrip antenna design. *International Journal of Antennas and Propagation*, 2013, 04 2013.

[8] Fei Ding, Jin Dai, Yiting Chen, Jianfei Zhu, yi jin, and Sergey Bozhevolnyi. Broadband near-infrared metamaterial absorbers utilizing highly lossy metals. *Scientific Reports*, 6:39445, 12 2016.

[9] Claire M. Watts, Xianliang Liu, and Willie J. Padilla. Metamaterial electromagnetic wave absorbers. *Advanced Materials*, 24(23):OP98–OP120, 2012, https://onlinelibrary.wiley.com/doi/pdf/10.1002/adma.201200674.

[10] V. G. Veselago. The Electrodynamics of Substances with Simultaneously Negative Values of $\in$ and μ. *Soviet Physics Uspekhi*, 10:509, Jan 1968.

[11] D. R. Smith, Willie J. Padilla, D. C. Vier, S. C. Nemat-Nasser, and S. Schultz. Composite medium with simultaneously negative permeability and permittivity. *Phys. Rev. Lett.*, 84:4184–4187, May 2000.

[12] J. B. Pendry. Perfect cylindrical lenses. *Opt. Express*, 11(7):755–760, Apr 2003.

[13] D. Schurig, J. J. Mock, B. J. Justice, S. A. Cummer, J. B. Pendry, A. F. Starr, and D. R. Smith. Metamaterial electromagnetic cloak at microwave frequencies. *Science*, 314(5801):977–980, 2006, https://science.sciencemag.org/content/314/5801/977.full.pdf.

[14] R. A. Shelby, D. R. Smith, and S. Schultz. Experimental verification of a negative index of refraction. *Science*, 292(5514):77–79, 2001, https://science.sciencemag.org/content/292/5514/77.full.pdf.

[15] Xianliang Liu, Tatiana Starr, Anthony F. Starr, and Willie J. Padilla. Infrared spatial and frequency selective metamaterial with near-unity absorbance. *Phys. Rev. Lett.*, 104:207403, May 2010.

[16] Hao Wang and Liping Wang. Perfect selective metamaterial solar absorbers. *Opt. Express*, 21(S6):A1078–A1093, Nov 2013.

[17] Na Liu, Martin Mesch, Thomas Weiss, Mario Hentschel, and Harald Giessen. Infrared perfect absorber and its application as plasmonic sensor. *Nano letters*, 10:2342–8, 07 2010.

[18] Thomas Maier and Hubert Brückl. Wavelength-tunable microbolometers with metamaterial absorbers. *Opt. Lett.*, 34(19):3012–3014, Oct 2009.

[19] Thomas Maier and Hubert Brueckl. Multispectral microbolometers for the midinfrared. *Opt. Lett.*, 35(22):3766–3768, Nov 2010.

[20] Barry P. Rand, Peter Peumans, and Stephen R. Forrest. Long-range absorption enhancement in organic tandem thin-film solar cells containing silver nanoclusters. *Journal of Applied Physics*, 96(12):7519–7526, 2004, https://doi.org/10.1063/1.1812589.

[21] N. I. Landy, C. M. Bingham, T. Tyler, N. Jokerst, D. R. Smith, and W. J. Padilla. Design, theory, and measurement of a polarization-insensitive absorber for terahertz imaging. *Phys. Rev. B*, 79:125104, Mar 2009.

[22] Irina Puscasu and William L. Schaich. Narrow-band, tunable infrared emission from arrays of microstrip patches. *Applied Physics Letters*, 92(23):233102, 2008, https://doi.org/10.1063/1.2938716.

[23] Xianliang Liu, Talmage Tyler, Tatiana Starr, Anthony F. Starr, Nan Marie Jokerst, and Willie J. Padilla. Taming the blackbody with infrared metamaterials as selective thermal emitters. *Phys. Rev. Lett.*, 107:045901, Jul 2011.

[24] James Grant, Yong Ma, Shimul Saha, Ata Khalid, and David R. S. Cumming. Polarization insensitive, broadband terahertz metamaterial absorber. *Opt. Lett.*, 36(17):3476–3478, Sep 2011.

[25] Qi-Ye Wen, Huai-Wu Zhang, Yun-Song Xie, Qing-Hui Yang, and Ying-Li Liu. Dual band terahertz metamaterial absorber: Design, fabrication, and characterization. *Applied Physics Letters*, 95(24):241111, 2009, https://doi.org/10.1063/1.3276072.

[26] Qianjun Mao, Chunzao Feng, and Yizhi Yang. Design of tunable multi-band metamaterial perfect absorbers based on magnetic polaritons. *Plasmonics*, 14:1–8, 07 2018.

[27] Jin Woo Park, Pham Van Tuong, Joo Yull Rhee, Ki Won Kim, Won Ho Jang, Eun Ha Choi, Liang Yao Chen, and YoungPak Lee. Multi-band metamaterial absorber based on the arrangement of donut-type resonators. *Opt. Express*, 21(8):9691–9702, Apr 2013.

[28] Lei Zhao, Han Liu, Zhihong He, and Shikui Dong. Design of multi-narrowband metamaterial perfect absorbers in near-infrared band based on resonators asymmetric method and modified resonators stacked method. *Optics Communications*, 420:95–103, 2018.

[29] Yu Qian Ye, Yi Jin, and Sailing He. Omnidirectional, polarization-insensitive and broadband thin absorber in the terahertz regime. *J. Opt. Soc. Am. B*, 27(3):498–504, Mar 2010.

[30] Wei Ma, Yongzheng Wen, and Xiaomei Yu. Broadband metamaterial absorber at mid-infrared using multiplexed cross resonators. *Opt. Express*, 21(25):30724–30730, Dec 2013.

[31] Hong Dang, Cuong Nguyen Van, Dinh Hai Le, Tung Nguyen, Manh Cuong, Dac Tuyen, and Dinh Vu. Broadband metamaterial perfect absorber obtained by coupling effect. *Journal of Nonlinear Optical Physics Materials*, 26:1750036, 09 2017.

[32] Atsushi Ishikawa and Takuo Tanaka. Metamaterial absorbers for infrared detection of molecular self-assembled monolayers. *Scientific reports*, 5:12570, 2015.

[33] Zhigang Li, Liliana Stan, David A. Czaplewski, Xiaodong Yang, and Jie Gao. Wavelength-selective mid-infrared metamaterial absorbers with multiple tungsten cross resonators. *Opt. Express*, 26(5):5616–5631, Mar 2018.

[34] Mohammadamir Ghaderi, Ehsan Karimi Shahmarvandi, and Reinoud F. Wolffenbuttel. Cmos-compatible mid-ir metamaterial absorbers for out-of-band suppression in optical mems. *Opt. Mater. Express*, 8(7):1696–1707, Jul 2018.

[35] Hu Tao, Chris Bingham, Andrew Strikwerda, D. Pilon, David Shrekenhamer, N. Landy, Kebin Fan, Xin Zhang, Willie Padilla, and Richard Averitt. Highly flexible wide angle of incidence terahertz metamaterial absorber: Design, fabrication, and characterization. *Physical Review B*, 78:241103(R), 12 2008.

[36] Fei Ding, Yanxia Cui, Xiaochen Ge, Yi Jin, and Sailing He. Ultra-broadband microwave metamaterial absorber. *Applied Physics Letters*, 100(10):103506, 2012, https://doi.org/10.1063/1.3692178.

[37] Joshua Hendrickson, Junpeng Guo, Boyang Zhang, Walter Buchwald, and Richard Soref. Wideband perfect light absorber at midwave infrared using multiplexed metal structures. *Opt. Lett.*, 37(3):371–373, Feb 2012.

[38] Ehsan Karimi Shahmarvandi, Mohammadamir Ghaderi, N. Pelin Ayerden, Ger de Graaf, and Reinoud F. Wolffenbuttel. CMOS-compatible metamaterial-based wideband mid-infrared absorber for microspectrometer applications. In Allan D. Boardman, Nigel P. Johnson, Kevin F. MacDonald, and Ekmel Özbay, editors, *Metamaterials X*, volume 9883, pages 30 – 38. International Society for Optics and Photonics, SPIE, 2016.

[39] Wei Ma, Yongzheng Wen, and Xiaomei Yu. Broadband metamaterial absorber at mid-infrared using multiplexed cross resonators. *Opt. Express*, 21(25):30724–30730, Dec 2013.

[40] James Clerk Maxwell. Viii. a dynamical theory of the electromagnetic field. *Philosophical Transactions of the Royal Society of London*, 155:459–512, 1865, https://royalsocietypublishing.org/doi/pdf/10.1098/rstl.1865.0008.

[41] D. R. Smith, D. C. Vier, Th. Koschny, and C. M. Soukoulis. Electromagnetic parameter retrieval from inhomogeneous metamaterials. *Phys. Rev. E*, 71:036617, Mar 2005.

[42] Yang Liu, Yitung Chen, Jichun Li, Tzu chen Hung, and Jianping Li. Study of energy absorption on solar cell using metamaterials. *Solar Energy*, 86(5):1586 – 1599, 2012.

[43] F. Bayatpur and K. Sarabandi. Single-layer high-order miniaturized-element frequency-selective surfaces. *IEEE Transactions on Microwave Theory and Techniques*, 56(4):774–781, April 2008.

[44] P. H. Q. Pham, Y. Wang, P. Burke, W. Zhang, and E. Brown. Towards perfect impedance matching of free space to a 2d material. In *2014 9th European Microwave Integrated Circuit Conference*, pages 676–678, Oct 2014.

[45] W. Shi, S. Liu, B. Zheng, X. Kong, H. Zhang, and S. Liu. Broadband perfect metamaterial absorption, based on flexible material. In *2016 IEEE International Workshop on Electromagnetics: Applications and Student Innovation Competition (iWEM)*, pages 1–3, May 2016.

[46] Aleksandar D. Rakić, Aleksandra B. Djurišić, Jovan M. Elazar, and Marian L. Majewski. Optical properties of metallic films for vertical-cavity optoelectronic devices. *Appl. Opt.*, 37(22):5271–5283, Aug 1998.

[47] Bingxin Zhang, Yanhui Zhao, Qingzhen Hao, Brian Kiraly, Iam-Choon Khoo, Shufen Chen, and Tony Jun Huang. Polarization-independent dual-band infrared perfect absorber based on a metal-dielectric-metal elliptical nanodisk array. *Opt. Express*, 19(16):15221–15228, Aug 2011.

[48] Viktor A Podolskiy, Andrey K Sarychev, Evgenii E Narimanov, and Vladimir M Shalaev. Resonant light interaction with plasmonic nanowire systems. *Journal of Optics A: Pure and Applied Optics*, 7(2):S32–S37, jan 2005.

[49] Govind Dayal and S. Anantha Ramakrishna. Design of highly absorbing metamaterials for infrared frequencies. *Opt. Express*, 20(16):17503–17508, Jul 2012.

[50] Dongju Lee, Jung Hwang, Daecheon Lim, Tadayoshi Hara, and Sungjoon Lim. Incident angle- and polarization-insensitive metamaterial absorber using circular sectors. *Scientific Reports*, 6:27155, 06 2016.

[51] Li Huang, Dibakar Roy Chowdhury, Suchitra Ramani, Matthew T. Reiten, Sheng-Nian Luo, Abul K. Azad, Antoinette J. Taylor, and Hou-Tong Chen. Impact of resonator geometry and its coupling with ground plane on ultrathin metamaterial perfect absorbers. *Applied Physics Letters*, 101(10):101102, 2012, https://doi.org/10.1063/1.4749823.

[52] Junqiao Wang, Chunzhen Fan, Pei Ding, Jinna He, Yongguang Cheng, Weiqin Hu, Genwang Cai, Erjun Liang, and Qianzhong Xue. Tunable broad-band perfect

absorber by exciting of multiple plasmon resonances at optical frequency. *Opt. Express*, 20(14):14871–14878, Jul 2012.

[53] Tianhua Meng, Dan Hu, and Qiaofen Zhu. Design of a five-band terahertz perfect metamaterial absorber using two resonators. *Optics Communications*, 415:151 – 155, 2018.

[54] Xiaopeng Shen, Tie Jun Cui, Junming Zhao, Hui Feng Ma, Wei Xiang Jiang, and Hui Li. Polarization-independent wide-angle triple-band metamaterial absorber. *Opt. Express*, 19(10):9401–9407, May 2011.

[55] Na Liu, Liwei Fu, Stefan Kaiser, H. Schweizer, and Harald Giessen. Plasmonic building blocks for magnetic molecules in three-dimensional optical metamaterials. *Advanced Materials*, 20:3859 – 3865, 10 2008.

[56] Jiangfeng Zhou, Lei Zhang, Gary Tuttle, Thomas Koschny, and Costas M. Soukoulis. Negative index materials using simple short wire pairs. *Phys. Rev. B*, 73:041101, Jan 2006.

Appendix A

Acronyms

A.1 Acronyms

Table A.1: Acronyms

Acronym	Meaning
TE	Transverse Electric
TM	Transverse Magnetic
THz	Terahertz ($1x10^{12}Hz$)
$\overrightarrow{E}$	Electric Field Intensity ($V.m^{-1}$)
$\overrightarrow{H}$	Magnetic Field Intensity ($A.m^{-1}$)
$\overrightarrow{D}$	Electric Flux Density (C/m^2)
$\overrightarrow{B}$	Magnetic Flux Density (Wb/m^2)
$\overrightarrow{J}$	Electric Current Density (A/m)
$\overrightarrow{S}$	Complex Poynting Vector
ρ	Volume charge density (C/m^3)
ε	Electric permittivity
μ	Magnetic permeability
ω	Angular frequency
k	Electromagnetic wave vector

Continued on next page

Table A.1 – continued from previous page

Acronym	Meaning
c	Speed of light
n	Refractive index
FEM	Finite Element Method
Z	Impedance
$A(w)$	Frequency dependent Absorbance
$R(w)$	Frequency dependent Reflectance
$T(w)$	Frequency dependent Transmittance
σ	Conductivity